Computational Modeling and Characterization of Amorphous Materials

A dissertation presented to

the faculty of

the College of Arts and Sciences of Ohio University

In partial fulfillment

of the requirements for the degree

Doctor of Philosophy

Dale J. Igram

December 2019

This dissertation titled

Computational Modeling and Characterization of Amorphous Materials

by

DALE J. IGRAM

has been approved for

the Department of Physics and Astronomy

and the College of Arts and Sciences by

David A. Drabold

Distinguished Professor of Physics and Astronomy

Florenz Plassmann

Dean, College of Arts and Sciences

Abstract

IGRAM, DALE J., Ph.D., December 2019, Physics

Computational Modeling and Characterization of Amorphous Materials (73 pp.)

Director of Dissertation: David A. Drabold

Two different materials, a non-glass former (*a*-Si) and a glass former ($Ag_{0.2}(Ge_{35}Se_{65})_{0.8}$), were considered for investigation. New structural models of these systems were obtained using state of the art methods. Several physical, electrical, and dynamical attributes of these materials were computed, which revealed atomistic structure, vibrational, electronic and transport properties.

To create high-quality continuous random network models of *a*-Si is difficult using conventional methods. A recently developed algorithm, force-enhanced atomic refinement (FEAR), has shown to provide excellent models. To illustrate this, an investigation was performed with respect to the structural, electronic, and vibrational properties of amorphous silicon, which consisted of several model types of different sizes that were constructed from melt-quench (MQ) and FEAR methods. The results from the FEAR models, as compared to the MQ models, correlated more closely with experiment, even for relatively large structure sizes. In addition, FEAR is generally about a factor of 10 faster than conventional methods.

Next, we investigated the static and dynamical properties of a ternary glassy material $Ag_{0.2}(Ge_{35}Se_{65})_{0.8}$ using *ab initio* molecular dynamics (AIMD). The results indicated the host network to be rigid and that additional substructures exist in the model. The radial distribution function of the $Ag_{0.2}(Ge_{35}Se_{65})_{0.8}$ model revealed reasonably good agreement with experiment. It has been shown that the model consists of $Ge(Se_{1/2})_4$ tetrahedra which are quite distorted from ideal. To better comprehend the dynamical properties of this model we performed a detailed analysis of the vibrational modes, which we believe to be a first for such a system. Finally, we examined A_1 breathing modes of the corner-sharing

tetrahedra where we affirm that these breathing modes are non-local and involve the mixing of modes for different symmetry which results in two bands of A_1 breathing modes, thus emphasizing the fact that local molecular vibration modes is an oversimplified approximation for amorphous materials.

Dedication

To my wife, Esperanza, all my family members, and in loving memory of my parents

Acknowledgements

My academic endeavor at Ohio University was a very memorable one, which could not have been accomplished without the support and understanding of several kind and thoughtful individuals. I would like to express my utmost appreciation to all these individuals during my academic career.

My most sincere appreciation is bestowed upon my advisor, Dr. David Drabold for the opportunity to perform interesting research under his leadership resulting in a deep appreciation for the hard work required for obtaining this degree. His guidance and assistance has helped me achieve what seemed, at times, an unattainable goal.

I would like to give special thanks to my other committee members, Drs. Chen and Nance, for their support, helpful suggestions, and review of this dissertation. A very special acknowledgement is given to Dr. Ingram for his unwavering support and encouraging words, and Dr. Castillo for providing guidance as a coauthor. In addition, I would like to acknowledge those individuals for which I had the opportunity to do teaching assistance with and for the professional development.

It would behoove me to provide thanks to all my former and current group members, Dr. Anup Pandey, Dr. Kiran Prasai, Dr. Bishal Bhattarai, Kashi Subedi, and Rajendra Thapa for their helpful discussions and friendships. It would be amiss not to give thanks to my other student colleagues and friends, Tomas Rojas Solorzano, Ruhi Thorat, Nilaj Chakrabarty, Ali Khaledi Nasab, and Oscar Avalos for all their support. My appreciation is given to all collaborators involved in my research for constructive conversations. I would also like to thank the many individuals in the Department of Physics and Astronomy, and Ohio University, in general, for making this dream of mine come true.

Finally, I extend my most sincere gratitude to my wife and family for all their endless support, patience and encouragement throughout the years while I embarked on this journey. I could not have done it without them.

Table of Contents

List of Tables

List of Figures

1 INTRODUCTION

Recently, there has been increasing interest in amorphous materials, because of their potential technological applications and also the lack of understanding of these materials, whose properties are quite different from crystalline materials [1]. Some of their properties can vary from one sample to the next with same material. An ideal crystal has translational order in all three dimensions, this is not true for an amorphous material because of imperfections and disorder.

A crucial distinction between an amorphous material and a crystal involves long-range order. A crystal has long-range order, whereas an amorphous material does not. This lack of long-range order is due to variation in bond lengths, bond angles and coordination numbers at individual atoms. This type of disorder is considered in this dissertation. The amount of short-range order that a structure has determines the extent of its topological disorder [2] . Direct inversion of structure from diffraction measurements is difficult because the data is averaged over macroscopic volumes and is smooth, carrying limited information about the structure.

A quantity that is commonly obtained from diffraction experiments is the radial distribution function (RDF). The RDF is a one-dimensional (1D) representation of a three-dimensional (3D) structure resulting in only a limited amount of structural information, thus the importance of structural modeling. Through the utilization of computational methods, structural modeling can contribute significantly to the understanding of an amorphous material by providing information on the structural parameters, such as pair correlation function (PCF), structure factor, radial distribution function (RDF), etc. To illustrate the utility of structural modeling to unveil the structure of amorphous systems, two different materials considered for study: amorphous silicon, and a silver-doped chalcogenide glass.

1.1 Amorphous Silicon

There are several technological applications where amorphous silicon (*a*-Si) and its hydrogenated version (*a*-Si:H) are utilized. While a number of traditional and non-traditional methods have been used to analyze these materials, most have not been totally successful.

The availability of high-precision experimental data from diffraction, infrared (IR), and nuclear magnetic resonance (NMR) has provided special opportunities for developing methods that can directly employ this data into structural modeling. An example of such a method is the reverse Monte Carlo (RMC) method (refer to section 1.3.2). However, this method has a major problem in which it creates unphysical structures when using diffraction data only, since it includes no chemical information.

The development of hybrid approaches, which maintain the character of RMC with respect to incorporating experimental data in simulations but also includes a cost function, has helped to resolve the problems associated with the direct (RMC) inversion of experimental data. One such hybrid method is the force-enhanced atomic refinement (FEAR) which has successfully incorporated experimental information in atomic simulations for creating structures that are consistent with both theory and experiments. The FEAR method has been utilized extensively, as shown in Chapter 2, for creating large and realistic models of *a*-Si consisting of up to 1000 atoms, which displayed excellent structural, electronic, and vibrational properties as compared to currently published RMC and *ab initio* molecular dynamics models.

1.2 Silver-doped Chalcogenide Glass

It was discovered in the mid-1960s [3] that incorporating silver into chalcogenide glasses produced new materials with special properties resulting in applications in the areas of optics, optoelectronics, and biology [4]. The $Ag_y(Ge_xSe_{1-x})_{1-y}$ system has been

studied extensively over the years both for academic and technological reasons. Computer simulations [5–8] have been performed in order to better understand the structural, electronic and silver ion dynamics of these systems.

Due to interest as a CBRAM computer memory material, the amorphous $Ag_{0.2}(Ge_{35}Se_{65})_{0.8}$ structure was modeled to better comprehend its static and dynamic properties, which is of great interest to engineers devising new CBRAM memory. Also, this composition has not been previously evaluated. In addition to the evaluation of structural, electronic, ion dynamics properties of the $Ag_{0.2}(Ge_{35}Se_{65})_{0.8}$ structure, an extensive investigation of the vibrational properties was studied.

1.3 Computational Methods

1.3.1 Ab initio Methods

It is desirable to reproduce experimental data and better to have some predictive ability. Structural modeling with computer simulations based on the first principles of quantum mechanics, independent of empirical parameters, can come close to achieving this. Because it is impossible to obtain an exact solution to the Schrodinger equation for a many-body system consisting of nuclei and ions, approximations [9] have been developed. Perhaps the most successful approximation is the density functional theory (DFT) which is a single particle approximation. This theory can determine the properties of a many-electron system by using functionals that are spatially dependent on election density.

It is well known that DFT has a limitation in that its exact functionals for exchange and correlation are not known except for the free electron gas [10]. Nevertheless, for electronic ground state properties and structural properties highly successful approaches are available. The most commonly used approximation or functional is the local-density approximation (LDA) [11], which depends only on the electronic density at the coordinate where the functional is evaluated. Another functional that is frequently used is the

generalized gradient approximation (GGA) [12]. The GGA functional considers the density and density gradient. Two well known *ab initio* DFT codes which were utilized in the research projects are discussed in the following sections.

1.3.1.1 Vienna Ab initio Simulation Package (VASP)

VASP is a computer package where *ab initio* quantum-mechanical Born-Oppenheimer molecular dynamics (MD) simulations are performed using pseudo-potentials[13] or the projector-augmented wave (PAW) method [14] and a plane wave basis set. The interactions between electrons and ions are described using ultra-soft pseudo-potentials or the projector-augmented-wave method. VASP provides an approximate solution to the many-body Schrdinger equation within the density functional theory (DFT) by solving the Kohn-Sham equations [15]. The electronic groundstate is determined by using an efficient iterative matrix diagonalization technique [16]. Forces on the atoms are calculated by evaluating the partial derivative of the free energy with respect to the atomic positions. Because atomic displacements are determined by VASP phonon calculations can be performed.

1.3.1.2 Spanish Initiative for Electronic Simulations with Thousand of Atoms (SIESTA)

SIESTA [17] is both a method and computer program designed to perform electronic structure calculations and *ab initio* molecular dynamics simulations of molecules and solids. The standard Kohn-Sham self-consistent DFT method in the local density (LDA-LSD) and generalized gradient (GGA) approximations, as well as in a nonlocal functional that includes van der Waals interactions (VDW-DF) are utilized by SIESTA. Atomic orbitals are used as a basis set, which allows multiple-zeta, polarization and off-site orbitals to be considered. The radial shape of every orbital is numerical and any shape may be considered by the user, only under the condition that it has finite support, in

other words, it has to be zero beyond a user-provided distance with respect to the associated nucleus. These flexible basis sets are the means for calculating the Hamiltonian and overlap matrices. SIESTA has some of the same features as VASP with regards to calculating the following: total and partial energies, atomic forces, stress tensor, electron density, geometry relaxation (fixed or variable cell), constant-temperature molecular dynamics (Nose thermostat), vibrations (phonons), and band structure.

1.3.2 Hybrid RMC Methods

The Reverse Monte Carlo (RMC) modeling method is a variation of the standard Metropolis-Hastings algorithm [18] for solving an inverse problem, whereby a model is adjusted until its parameters have the greatest correlation with experimental data. For condensed matter problems, the RMC method was initially developed by McGreevy and Pusztai [19] in 1988, with application to liquid argon. RMC alone will not produce a realistic structure of amorphous materials when using diffraction data only [19, 20]. This method has always confronted some amount of controversy, the most common criticism is that RMC does not provide a unique solution. Other approaches utilizing the RMC method have been formulated, such as Experimentally Constrained Molecular Relaxation (ECMR) [21], a hybrid RMC (HRMC) utilizing empirical forces [22], a combination of a liquid-quench procedure and a HRMC concept [23], an Invariant Environment Refinement Technique [24], and a Seed Coordinate Anneal (SCA) method [25]. However, a recently developed hybrid algorithm, force enhanced atomic refinement (FEAR), has been utilized successfully for different amorphous materials (a-Si, a-SiO_2, and a-C), which is discussed next.

1.3.2.1 Force-Enhanced Atomic Refinement (FEAR)

FEAR is a structural modeling method that utilizes RMC for the fitting of experimental data and incorporates inter-atomic forces, obtained by the total-energy

functional, to minimize the total energy and forces in a self-consistent way. A flow diagram is illustrated in Fig. 1.1.

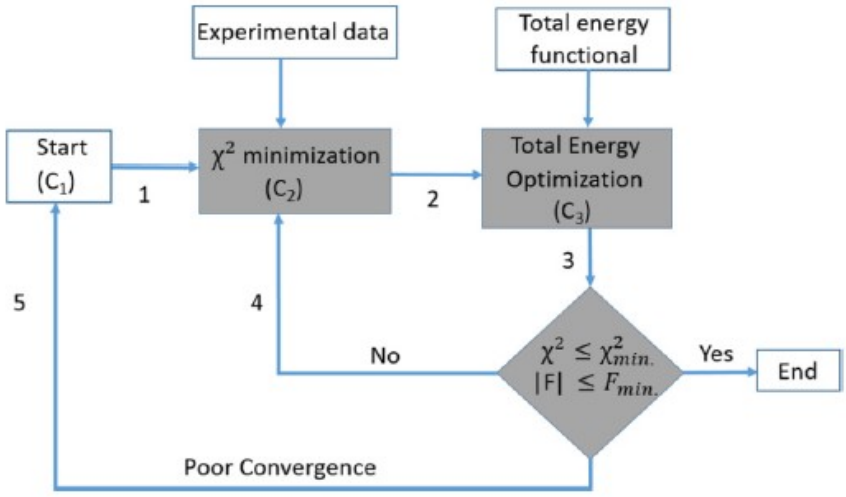

Figure 1.1: Pictorial of the FEAR algorithm [26].

The FEAR algorithm consists of the following steps: starting with an initial configuration (C_1), which is usually random; the atomic coordinates from the initial configuration is passed (path 1) to the RMC algorithm; the RMC algorithm uses these coordinates to perform a partial fit to experimental data producing a new configuration (C_2); the new coordinates are incorporated into the total energy optimization process (path 2) where a gradient-descent method is used resulting in a configuration (C_3), which is then evaluated (path 3) with respect to criteria for χ^2 and force; the self-consistent process is continued (paths 2 to 3 to 4 to 2) until the convergence criteria are satisfied. The C_3 structure is then fully relaxed resulting in the final structure. The function to minimize is

$$\chi^2 = \sum_i \left[\frac{F_E(k_i) - F_C(k_i)}{\sigma(k_i)} \right]^2 \tag{1.1}$$

where $F_{E/C}(k_i)$ represent the experimental/configurational structure factors and $\sigma(k_i)$ the experimental error related to the data for wave vector k_i . The efficiency of the FEAR algorithm is due to the partial use of RMC and ab initio MD relaxation for each FEAR step. Empirically, an acceptable ratio of RMC steps to relaxation steps for good efficiency and efficacy is about 100:1, which is advantageous, since the RMC calls are computationally inexpensive for amorphous materials.

1.4 Structural Properties

Scattering experiments are performed to discover partial information about the structure of matter. From an atomistic view, the purpose of structural analysis is to relate the structure to the properties of real materials so that they can be better understood. This understanding can lead to an improvement of the material or development of new ones with better properties. Some of the most commonly utilized quantities in structural analyzes are described in the following sections.

1.4.1 Static Structure Factor

The static structure factor, $S(Q)$, obtained from neutron, electron or X-ray diffraction experiments, is defined [27] as

$$S(Q) = 1 + \frac{1}{Q}\int_0^\infty G(r)sin(Qr)dr \tag{1.2}$$

where Q represents the diffraction vector and $G(r)$ the reduced pair distribution function. $G(r)$ is most directly associated with the experimental data because it is obtained precisely from the Fourier transform of $S(Q)$ and is written as

$$G(r) = 4\pi r\rho_o(g(r) - 1) \tag{1.3}$$

where $g(r)$ is the pair distribution or pair correlation function.

1.4.2 Pair Correlation Function

The pair correlation function *g(r)*, also known as pair distribution function (PDF), is related to the pair density function by $\rho(r) = \rho_o g(r)$, where ρ_o represents the average number density for the material. From Fig. 1.2, it is shown that as $r \to \infty$, $\rho(r) \to 1$. Also revealed are oscillations of $\rho(r)$ where for large r, $\rho(r)$ asymptotes to ρ_o, and becomes zero as $r \to 0$. These functions can affirm the small-r short-range order.

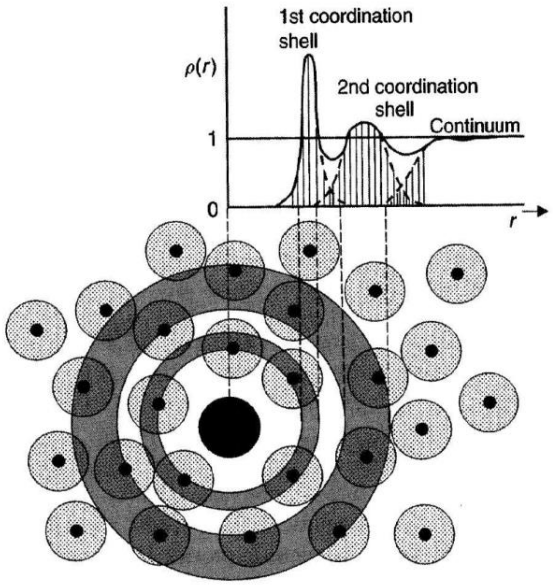

Figure 1.2: Illustration of the density function $\rho(r)$ for an amorphous material [10].

A PDF peak can provide the following information [27]: the peak position provides the average atomic pair distance, the peak integrated intensity gives the coordination number of the atomic pair, and the width and shape of the peak can yield the atomic probability distribution.

1.4.3 Radial Distribution Function

The most intuitive distribution function is the radial distribution function (RDF) [27], which defined as

$$R(r) = 4\pi r^2 \rho_o g(r) \tag{1.4}$$

The quantity $R(r)$ can be used to provide the number of atoms in an annulus of thickness dr at a distance of r from another atom, as shown in Fig. 1.2. The number of neighboring atoms, N_C, is written as

$$N_C = \int_{r_1}^{r_2} R(r) dr \tag{1.5}$$

where r_1 and r_2 represents the RDF peak associated with the coordination shell (defined by r_1 and r_2) under consideration. This quantity is also considered as the coordination number.

1.4.4 Ring Statistics

Ring statistics, which is based on graph theory, is the analysis of topological networks (liquid, crystalline or amorphous structures) involving the connectivity of structural information which can be used by representing nodes for atoms and links for bonds [10]. If a series of nodes and links are connected sequentially with no overlap then it is called a path. A ring is considered a closed path. A N-membered ring is a ring with N nodes. If a particular node of a network is evaluated we may see that this node is associated with a number of rings, where each of these rings can be defined by its size and classified based on the relations between nodes and links that is composing it.

There are a couple of methods for determining ring sizes. The first method involves using the total number of nodes of the ring (i.e. N-membered ring is a ring consisting of N

nodes) and the other method relies on using the total number of network-forming nodes. The first method was utilized for the work presented in this dissertation.

Different criteria exists to classify rings, for details see [28]. One of the most commonly used criterion is the King shortest path criterion [29], which was used for the work contained in this dissertation. The King criterion is depicted in Fig. 1.3.

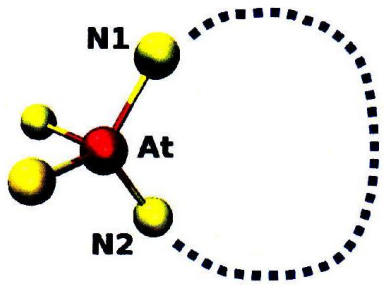

Figure 1.3: King criterion: a ring representing the shortest path between two of the nearest atoms (N1 and N2) of a given node (At) [29].

The King criterion defines a ring as the shortest path which comes back to a given node from one of its nearest neighbors.

1.5 Electronic Properties

Promising electronic materials [30] with a wide range of applications such as solar cells, thin-film transistors, light sensors, optical memory devices, vidicons, electrophotographic applications, and x-ray image sensors are fabricated from amorphous semiconductors. The applications of these materials are dependent on the material's electronic properties. Two important quantities for characterizing the electronic structure of these materials are electronic density of states (EDOS) and electronic localization, which will be discussed next.

1.5.1 Electronic Density of States

The electronic density of states is a fundamental physical quantity which can be indirectly examined with photo-emission and optical absorption experiments. Because amorphous materials lack periodicity, unlike a crystalline solid, electrons cannot be described by Bloch states and a band structure having the form $E(k)$. A quantity that can equally represent electron states for both crystalline and amorphous materials is the density of states [2], defined as

$$g(E) = \frac{1}{N_{basis}} \sum_{i=1}^{N_{basis}} \delta(E - E_i) \tag{1.6}$$

where $g(E)$ represents the density of states per unit volume per energy interval, N_{basis} the number of basis orbitals, and E_i the eigenvalues. With respect to calculations, E_i represents the Kohn-Sham eigenvalues obtained from DFT calculations. Important information regarding energy gap and localized states near the Fermi energy can be obtained from EDOS which can reveal the shape of the band tails of a material. Of course, the gap is usually underestimated in DFT calculations - typically by a factor of ~ 2.

1.5.2 Electronic Localization

An important quantity for quantifying the localization of states is the inverse participation ratio (IPR), which provides valuable information of the localization of states regarding topological anomalies (defects, voids, etc) present in amorphous materials. IPR is written as

$$I_e(\psi_k) = \frac{\sum_{i=1}^{N} |a_i^k|^4}{(\sum_{i=1}^{N} |a_i^k|^2)^2} \tag{1.7}$$

where i represents atom i, ψ_k the kth eigenfunction, N the total number of atoms, and a_i^k the atomic orbital projection of atom i. A totally localized state is defined as $I_e(\psi_k)$ equal

to unity and for extended states, $I_e(\psi_k) \approx 1/\mathrm{N}$, where the wavefunctions are significantly overlapping, and are ideally extended.

1.6 Vibrational Properties

A dynamical model, one that considers the motion of atoms, can contribute valuable information on the thermodynamics of a material (e.g. thermal properties, thermal expansion, existence of phase transitions, etc.) where a static model cannot. Considering the dynamics of a material reveals a more complete picture of that material as a function of temperature. There are several quantities that are used to described the dynamical behavior of a material, and some of them are discussed below.

1.6.1 Vibrational Density of States

Vibrational density of states (VDOS) can provide fundamental information regarding the local bonding environment of amorphous materials and is defined [31] as

$$g(\omega) = \frac{1}{3N} \sum_{i=1}^{3N} \delta(\omega - \omega_i) \tag{1.8}$$

where N is the total number of atoms, $3N$ total number of phonon states, and ω phonon frequency. $g(\omega)$ is evaluated using a Gaussian broadening function for the delta function. The quantity $g(\omega)d\omega$ represents the number of phonon states or modes within an interval $(\omega, \omega + d\omega)$.

1.6.2 Vibrational Localization

Structural disorder existing within amorphous materials creates localized modes which can be characterized by the vibrational inverse participation ratio (VIPR). VIPR, similar to the electronic IPR, quantifies which normal modes are extended or localized. Following the notation of Zotov et al.[32], VIPR is defined as

$$I_v(p) = \frac{\sum_{i=1}^{N} |u_i^p|^4}{(\sum_{i=1}^{N} |u_i^p|^2)^2} \tag{1.9}$$

where u_i^p represents the eigenvector or displacement of atom i for a given mode p of frequency ω_p, which is summed over all atoms. A complete localization of the eigenvectors is characterized by I_v=1, whereas an extended state or de-localization when I_v is close to 0.

1.6.3 Stretching Character

Another important property is the stretching character [32, 33] which quantifies bond stretching or bending as determined by equation below

$$S(p) = \frac{\sum_{i,j} |(\boldsymbol{u}_i^p - \boldsymbol{u}_j^p) \cdot \hat{r}_{ij}|}{\sum_{i,j} |(\boldsymbol{u}_i^p - \boldsymbol{u}_j^p)|} \tag{1.10}$$

where $\hat{r}_{ij}$ represents a unit vector along the bond for atoms i and j. The summations are over all nearest-neighbor atom pairs (i,j) in the model. Its value will be close to +1 if the mode has prodominantly bond-stretching (compressing) characteristics and close to 0 if the mode has mostly bond-bending characteristics.

1.6.4 Phase Quotient

The character of the correlations between individual atomic displacements is obtained by considering the phase quotient q [34], as well as its parallel and perpendicular components, of the modes. This amounts to determining if the relative motion of neighboring atoms is in-phase (acoustic-like) or out-of-phase (optical-like) over the whole structure. For example, $q_{\|}(p)$ represents the projected motion that is parallel to the bonds and $q_{\perp}(p)$ the projected motion perpendicular to the bonds. These quantities are conveniently defined as

$$q(p) = \frac{\sum_{i,j} \boldsymbol{u}_i^p \cdot \boldsymbol{u}_j^p}{\sum_{i,j} |\boldsymbol{u}_i^p \cdot \boldsymbol{u}_j^p|}, \tag{1.11}$$

$$q_{\parallel}(p) = \frac{\sum_{i,j} \boldsymbol{u}_i^p \cdot (\hat{R}_{ij}\hat{R}_{ij}) \cdot \boldsymbol{u}_j^p}{\sum_{i,j} |\boldsymbol{u}_i^p \cdot (\hat{R}_{ij}\hat{R}_{ij}) \cdot \boldsymbol{u}_j^p|}, \tag{1.12}$$

$$q_{\perp}(p) = \frac{\sum_{i,j} \boldsymbol{u}_i^p \cdot (1 - \hat{R}_{ij}\hat{R}_{ij}) \cdot \boldsymbol{u}_j^p}{\sum_{i,j} |\boldsymbol{u}_i^p \cdot (1 - \hat{R}_{ij}\hat{R}_{ij}) \cdot \boldsymbol{u}_j^p|}. \tag{1.13}$$

Sums are again over all nearest-neighbor atom pairs (i,j) in the model. $\hat{R}_{ij}$ represents the unit vector in the direction of bond (i,j) and $\hat{R}_{ij}\hat{R}_{ij}$ a dyadic quantity.

1.6.5 Different Types of Atomic Motion

Different types of atomic motion [35] exist with regards to atoms of the host network and are quantified by

$$B_{\alpha}(p) = \frac{\sum_{i=1}^{N_\alpha} \boldsymbol{u}_i^p \cdot \hat{r}_b}{\sum_{i=1}^{N\alpha} |u_i^p|} \tag{1.14}$$

$$S_{\alpha}(p) = \frac{\sum_{i=1}^{N_\alpha} \boldsymbol{u}_i^p \cdot \hat{r}_s}{\sum_{i=1}^{N\alpha} |u_i^p|} \tag{1.15}$$

$$R_{\alpha}(p) = \frac{\sum_{i=1}^{N_\alpha} \boldsymbol{u}_i^p \cdot \hat{r}_r}{\sum_{i=1}^{N\alpha} |u_i^p|} \tag{1.16}$$

where α represents atomic type, $\hat{r}_b$ a unit vector parallel to the bisector of a three-atom angle, $\hat{r}_s$ an in-plane unit vector perpendicular to the bisector, and $\hat{r}_r$ a unit vector perpendicular to both. Summations are over all atoms of atomic type α. The quantities

$B_\alpha(p)$, $S_\alpha(p)$, and $R_\alpha(p)$ can all vary from +1 for complete bending, stretching, or rocking motion to zero and $B_\alpha(p)+S_\alpha(p)+R_\alpha(p)=1$ for each p.

1.6.6 Thesis Unity

In this dissertation, two archetypal amorphous materials are considered with similar modeling methods being applied to them. We will illustrate that realistic atomistic models of these materials can be achieved with the utilization of these methods. In addition, the application of plane-wave basis DFT and local atomic basis DFT can produce a likewise realistic representation of these two amorphous structures. We investigate the static and dynamical properties of these materials by using the quantities just described to reveal the atomistic structure, electronic, vibrational and transport characteristics. We perform a detailed study of the lattice dynamics of both amorphous materials resulting in many significant insights with respect to computational methods (MQ and FEAR) and ion motion for the silver-doped chalcogenide glass.

1.7 Blueprint of Dissertation

The remainder of the dissertation is organized in the following manner. Chapter 2 presents the computational methodology used to produce large and realistic models of amorphous silicon using the FEAR method. Verification of properties of the FEAR models with particular emphasis on the structural, electronic, vibrational, and thermal properties are presented and discussed. Chapter 3 describes the computational methodology used for creating a silver-doped chalcogenide glass model. The model and preparation methods are discussed, followed by a presentation and discussion of the structural, electronic, vibrational, and ion dynamics properties of the model. A detailed investigation of the vibrational properties of a silver-doped chalcogenide glass is a first, to the best of our knowledge.

2 Large and Realistic Models of Amorphous Silicon

The work presented in Chapter 2 has been published in Dale Igram, Bishal Bhattarai, Parthapratim Biswas, D.A. Drabold, Large and realistic models of amorphous silicon, *Journal of Non-Crystalline Solids*, **492** (2018) 27-32.

2.1 Introduction

Amorphous silicon (*a*-Si) and its hydrogenated counterpart (*a*-Si:H) continue to play an important role in technological applications, such as thin-film transistors, active-matrix displays, image-sensor arrays, multi-junction solar cells, multilayer color detectors, thin-film position detectors, etc [36]. While a number of traditional methods, based on Monte Carlo and molecular-dynamics simulations, were developed in the past decades by directly employing classical or quantum-mechanical force fields – from the event-based Wooten-Winer-Weaire (WWW) [37, 38] bond-switching algorithm and the activation-relaxation technique (ART) [39, 40] to the conventional melt-quench (MQ) molecular-dynamics simulations [41–46] – none of the methods utilize prior knowledge or experimental information in the simulation of atomistic models of complex materials. It is now widely accepted that dynamical methods perform rather poorly in generating high-quality (i.e., defect-free) continuous-random-network (CRN) models of amorphous silicon by producing too many coordination defects (e.g., 3- and 5-fold coordinated atoms) in the networks. While the WWW algorithm and the ART can satisfactorily address this problem by producing 100% defect-free CRN models of *a*-Si, a direct generalization of the WWW algorithm for multicomponent systems is highly nontrivial in the absence of sufficient information on the bonding environment of the atoms. Likewise, the ART requires a detailed knowledge of the local minima and the saddle points on a given potential energy surface in order to determine suitable low-lying minima that correspond to defect-free CRN models of amorphous silicon. On the other hand, the availability of

high-precision experimental data from diffraction, infrared (IR), and nuclear magnetic resonance (NMR) measurements provide unique opportunities to develop methods, based on information paradigm, where one can directly incorporate experimental data in simulation methodologies. The reverse Monte Carlo (RMC) method [47–50] is an archetypal example of this approach, where one attempts to determine the structure of complex disordered/amorphous solids by inverting experimental diffraction data. Despite its simplicity and elegance, the method produces unphysical structures using diffraction data only. While inclusion of appropriate geometrical/structural constraints can ameliorate the problem, the generation of high-quality models of *a*-Si, using constrained RMC simulations, has been proved to be a rather difficult optimization problem and satisfactory RMC models of *a*-Si have not been reported in the literature to our knowledge. The difficulty associated with the inversion of diffraction data using RMC simulations has led to the development of a number of hybrid approaches in the past decade [51, 52]. Hybrid approaches retain the spirit of the RMC philosophy as far as the use of experimental data in simulations is concerned but go beyond RMC by using an extended penalty function, which involves total energy and forces from appropriate classical/quantum-mechanical force fields, in addition to few structural or geometrical constraints. The experimentally constrained molecular relaxation [21, 53] (ECMR), the first-principle assisted structural solutions [54] (FPASS), and the recently developed force-enhanced atomic refinement [26, 55–57] (FEAR) are a few examples of hybrid approaches, which have successfully incorporated experimental information in atomistic simulations to determine structures consistent with both theory and experiments. Recently, the FEAR has been applied successfully to simulate amorphous carbon (*a*-C) [57]. This is particularly notable as the latter can exist in a variety of complex carbon bonding environment, which makes it very difficult to produce *a*-C from *ab initio* molecular-dynamics simulations due to the lack of *glassy* behavior and the WWW bond-switching algorithm in the absence of prior

knowledge of the bonding states of C atoms in *a*-C (e.g., the ratio of sp^2- versus sp^3-bonded C atoms with a varying mass density). In this chapter, we show that the information-based FEAR approach can be employed effectively to large-scale simulations of *a*-Si consisting of up to 1000 atoms. The resulting models have been found to exhibit superior structural, electronic, and vibrational properties of *a*-Si as far as the existing RMC and *ab initio* MD models are concerned in the literature.

2.2 Methodology and Models

For this study, three model sizes (216, 512 and 1024 atoms) were implemented with FEAR and compared with experimental data. Several algorithms and codes were utilized for the preparation of the models; namely, FEAR[26, 55, 56], RMCProfile[58], SIESTA[59] and VASP [60–62].

A random starting structure was constructed for each of the models and was refined by fitting to the experimental pair correlation functions $g(r)$ and/or the static structure factor $S(q)$ by employing RMCProfile. The refined structure is relaxed using conjugate gradient (CG) in SIESTA. The relaxed-refined structure is then refined by RMCProfile. This cyclic process is repeated until convergence is achieved. For completeness the converged structure is then fully relaxed by VASP (plane wave LDA).

The partial refinement steps in RMCProfile were carried out with a minimum distance between atoms of 2.10 $\mathring{A}$ and maximum move distance of 0.15 $\mathring{A}$ – 0.35 $\mathring{A}$. The partial relaxation steps utilized SIESTA with a single-ζ basis set, Harris functional at constant volume, exchange-correlation functional with local-density approximation (LDA), periodic boundary conditions and a single relaxation step. The final relaxation step employed VASP with a plane-wave basis set, plane-wave cutoff of 350 – 450 eV, energy difference criteria of 10^{-4} – 10^{-5}. The fully relaxed calculations were performed

for $\Gamma(\vec{k} = 0)$. For all the FEAR models, we have used structure factor data from *Laaziri et.al.* [63] for RMC refinement.

The three FEAR models and 216 MQ model have a number density of about 0.05005 atom/$\mathring{A}^3$, which is associated with atomic density of 2.33 g/cm^{-3} (details in Table I). The 216 MQ model was fabricated by taking a set of random coordinates and equilibrating these coordinates at 3000K for 6ps, followed by cooling from 3000K to 300K within 9 ps, then equilibration at 300K for 4.5 ps, and a full relaxation at 300K. The MQ calculations were performed with a step size of 1.5 fs. These are typical simulation times used to prepare accurate *ab initio* models for *a*-Si.[1]

We have also considered two large (4096 atom and 10,000 atom) WWW [37, 38] models in our comparison. These two WWW models were relaxed using SIESTA with a single-ζ basis set, LDA at constant volume utilizing Harris functional.[2]

2.3 Results

2.3.1 Structural Properties

A comparison of the structure factor for the six models 216 MQ, 216 FEAR, 512 FEAR, 1024 FEAR, 4096 WWW and 10,000 WWW models with respect to experiment [63, 67] is shown in Fig. 2.1.

From Fig. 2.1 (left panel) we can clearly observe that these models of up to 512 atoms are insufficient to resolve the first peak occurring at low q. In contrast, the 1024 FEAR model does well even in comparison to much larger models as seen in Fig. 1(right panel). This is also indicated in the real space information $g(r)$ (Fig. 2.2), where we

[1] It is worth noting that MQ is not a unique process, and it has recently been shown that very long anneals of a-Si can lead to models approaching WWW quality, contrary to the usual view that MQ only works for glass formers. These are very extended simulations however, and do not seem to be a very efficient way to model non-glass forming materials [64–66].

[2] We minimized our 4096 WWW model to a have forces less than 0.01 $eV/\mathring{A}$and for the 10,000 WWW model after $\sim$ 100 CG steps, RMS force of 0.024 $eV/\mathring{A}$ was obtained.

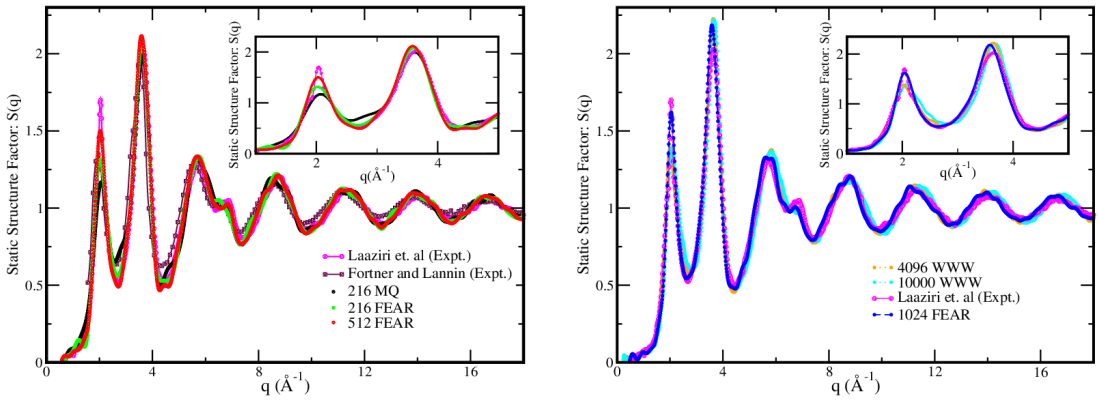

Figure 2.1: Structure factor for different models and their comparison with experiments [63, 67]. Inset: Plot of low q region of structure factor.

observed that the 10000 WWW model is slightly shifted as compared to the experiment [63] for the first and second neighbor peaks. We report the details of our simulation and important observables in Table 1.

From Table 1, we observe that there are some defects in our models. These structural defects arise due to a small fraction ($\sim 5\%$) of over co-ordinated and under co-ordinated atoms. This explains the fact that all of our models have coordination value slightly above the perfect four-fold coordination. Experimentally, it is also observed that a-Si does not posses a perfect four-fold coordination [63, 67]. Our final models obtained after relaxation attain energies (eV/atom) equal or less than models obtained from MQ.

We further show our plots of bond-angle distribution in Fig. 2.2 (right panel) to attest accuracy of FEAR models. As seen in Fig. 2.2, the peak of the bond angle is close to the ideal tetrahedral angle of 109.47^o. Similarly, from ring statistics (Fig. 2.3) we observed that these a-Si networks mostly prefer a ring size of 5,6,7. Small rings (mostly 3-membered rings) are responsible for an unrealistic peak seen in unconstrained RMC [55] at an angle around $\sim 60^o$. *Opletal et. al.* have proposed use of a constraint for removal of these highly constrained 3 membered rings in several of their works [51, 68].

Table 2.1: Nomenclature and details of our models: Length of the cubic box(L), position of first (r_1) and second (r_2) peak of RDF, Average coordination number (n), percentage of 3-fold, 4-fold and 5-fold coordinated atoms, Free Energy per atom of the final VASP relaxed models(E_0).

Model	L(Å)	r_1(Å)	r_2(Å)	n	3-fold %	4-fold %	5-fold%	$E_0(eV/atom)$
216MQ	16.28	2.36	3.81	4.083	0.93	87.03	11.57	0.000
216FEAR	16.28	2.36	3.81	4.028	1.39	94.44	4.17	-0.002
512FEAR	21.71	2.35	3.82	4.008	1.17	95.90	2.73	-0.044
1024FEAR	27.35	2.36	3.79	4.018	2.34	94.53	3.13	-0.035
4096WWW	43.42	2.36	3.78	4.004	0.05	99.46	0.49	—
10000WWW	57.32	2.31	3.69	4.014	0.04	98.60	1.30	—

The FEAR method, which incorporates accurate *ab initio* interactions, enables us to remove these high energy structures without satisfying an extra criterion.

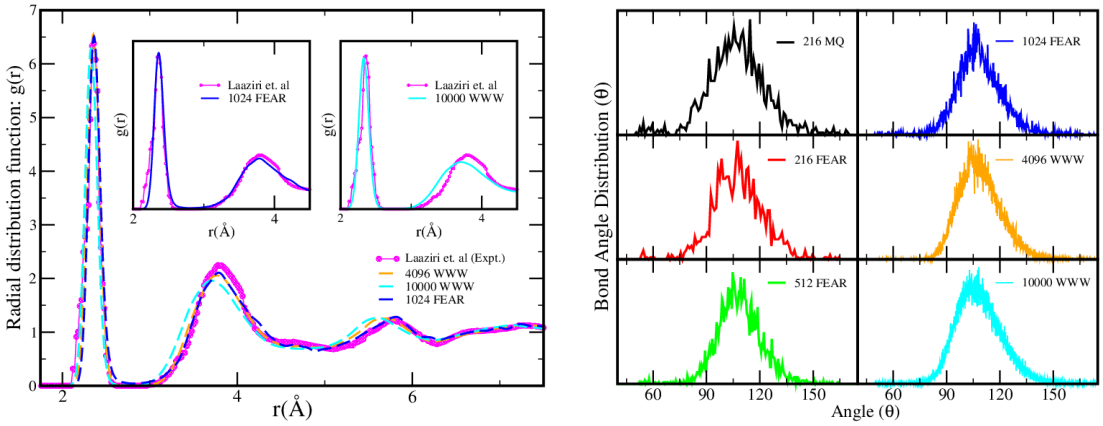

Figure 2.2: (left panel) Radial distribution function of different models and their comparison with experiment [63], Inset: Plot of *g(r)* of 1024 FEAR and 10,000 WWW models with experimental results, (right panel) Plot of bond-angle distribution for the six models.

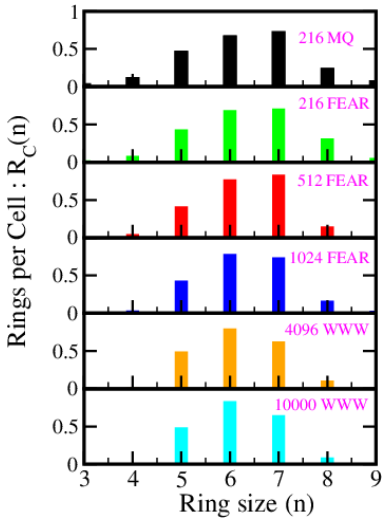

Figure 2.3: Rings per cell (R_C)for the six models. The ring statistics were obtained using the King's method [69] within ISAACS software [70].

2.3.2 Electronic Properties

Electronic properties, such as electronic density of states (EDOS), reveal crucial information regarding accuracy of models. In particular, *Prasai et. al.* and others [71, 72] have used electronic information to aid in modeling amorphous system. Conversely, EDOS obtained for our models validate accuracy of our models. We have shown plots of four models in Fig. 2.4. We have also studied the localization of electronic states by plotting the inverse participation ratio (IPR), using equation (1.7), in conjunction with EDOS. We observe plots with the same qualitative resemblance with a few localized states appearing near the Fermi energy ($E_F = 0$). These localized states arise due to the defects in the model (3-fold and 5-fold atoms).

We compare our large model of 4096 atoms along with our FEAR models. Due to the enormous size of this model, we have used Harris Functional and single-ζ basis set to evaluate the electronic density of states of these models. To the best of our knowledge this is a first time of reporting an *ab initio* based EDOS of *a*-Si models of this size.

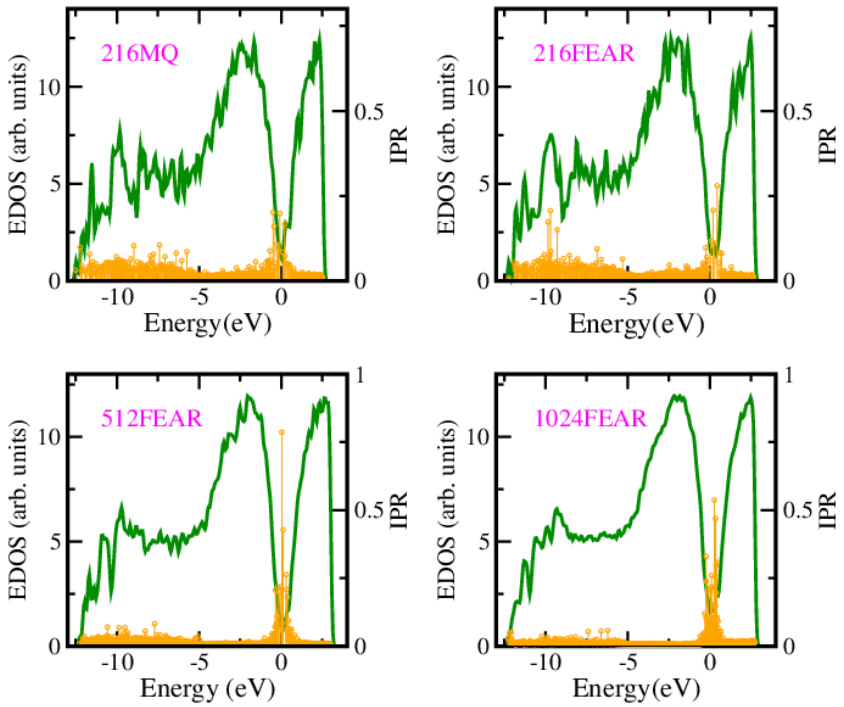

Figure 2.4: Plot of Electronic density of states (EDOS(E_F=0)) green-solid lines and Inverse participation ratio (IPR) yellow-drop lines.

2.3.3 Vibrational Properties

2.3.3.1 Vibrational Density of states

Vibrational density of states (VDOS) provides key information about the local bonding environments in amorphous solids. It is considered an important calculation to verifying the credibility of a model [73]. Meanwhile, it is equally challenging to get a good comparison of vibrational properties between theoretical and experimental results. Several factors like: model size, completeness of basis set etc. can affect vibrational properties. We have performed ionic-relaxation on our models to attain a local minimum with forces on each atom less than (~ 0.01 eV/atom), while simultaneously relaxing lattice vectors to zero pressure. This results in a slightly different number density and a non-orthogonal cell, but as shown in our earlier work [74], it is crucial to have coordinates

well relaxed before evaluating the vibrational properties of the models. We have computed vibrational properties for our four models(216 MQ, 216 FEAR, 512 FEAR and 1024 FEAR) using the dynamical matrix. We displaced each atom in 6-directions($\pm x$,$\pm y$,$\pm z$) with a small displacement of (~ 0.015 $\mathring{A}$). After each small displacement an *ab initio* force calculation was carried out to obtain a force constant matrix (for details see [75]).

We have computed the VDOS, using equation (1.8), for our models using the method of Gaussian broadening with a standard deviation of $\sigma = 1.86$ meV or 15.0 cm^{-1}. The first three zero frequency modes are due to supercell translations, and have been neglected during our calculations of VDOS and vibrational IPR. The VDOS results for our different models are illustrated in Fig. 2.5.

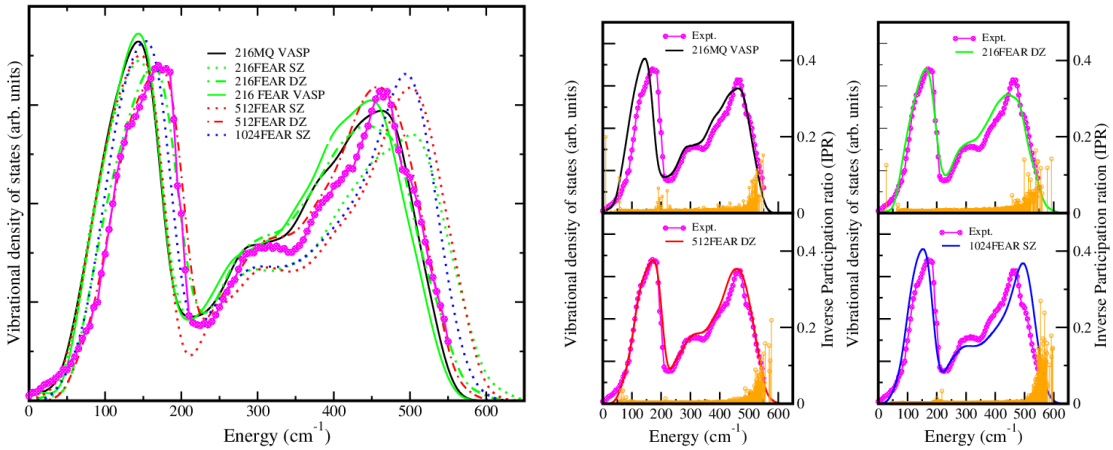

Figure 2.5: (left panel) Vibrational density of states (VDOS) obtained for different models using VASP-LDA, SIESTA-LDA(single-ζ, SZ) and SIESTA-LDA (double-ζ, DZ), (right panel) Comparison of vibrational density of states (VDOS) with experimental results [76] (Note the almost perfect agreement for the 512 DZ calculation). The yellow drop-lines shows inverse participation ratio (IPR), IPR measures localization of eigenmodes.

As seen in Fig. 2.5, there is a slight horizontal shift in VDOS depending upon system size and completeness of basis set. VDOS calculated with minimal basis set (single-ζ, SZ)

in SIESTA has a qualitative agreement with the experimental result, while a slight shift is observed at both low and high energies w.r.t the experiment. This result is refined by using a more complete basis-set (double-ζ, DZ), which gives a better agreement between our models and experiment. We have computed VDOS using DZ for two of our models (FEAR 216 and FEAR 512). The VDOS obtained for FEAR 512 is strikingly similar to the experiment (Fig.2.5, right panel). This switch from minimal basis to double ζ basis impacts computation time needed for these calculations and with our resources at hand we simply could not perform DZ calculations for our FEAR 1024 atom system.

Thus, we can infer that the completeness of basis-set affects these low energy excitation of atoms in amorphous silicon. The most remarkable feature is the improvement at high frequencies. Based on our zero pressure (double-ζ, DZ) calculation, it's agreement with experimental VDOS and specific heat (Fig. 2.6), we obtained a new density for *a*-Si. Our results are tabulated in Table II. Note that our results for the zero pressure (double-ζ, DZ) calculation are close to the experimental density for *a*-Si (2.28 g/cm^3) [77].

Table 2.2: Details of densities obtained after zeropressure relaxation of FEAR models for single-ζ (SZ) and double-ζ(DZ) basis sets in SIESTA. Our density for zero pressure (DZ) is closer to the experimental density of 2.28 g/cm^3[77].

Models	Volume(Å^3)	N($atom$/Å^3)	$\rho(g/cm^3)$
216 FEAR(SZ)	4643.77	0.046514	2.16
512 FEAR(SZ)	10997.33	0.046557	2.17
1024 FEAR(SZ)	21755.17	0.047067	2.19
216 FEAR (DZ)	4510.57	0.047887	2.23
512 FEAR(DZ)	10652.76	0.048062	2.24
1024 FEAR(DZ)	21213.92	0.048270	2.25

Structural disorder in amorphous solids lead to localized modes and these localized modes were evaluated by using equation (1.9) for the inverse participation ratio (IPR). We

plotted IPR for our four models in Fig.2.5 (right panel). The vibrations at low energies are mostly extended modes, these represent mostly bending type while vibrations at higher energies are dominated by stretching type of modes [74, 75].

2.3.3.2 Specific Heat in the harmonic approximation

We evaluated the specific heat in the harmonic approximation using the vibrational density of states $g(\omega)$ information obtained from our models. We compute the specific heat $C_v(T)$ from the relation [78]

$$C(T) = 3R \int_0^{E_{max}} \left(\frac{E}{k_B T}\right)^2 \frac{e^{E/k_B T}}{\left(e^{E k_B T} - 1\right)^2} g(E) dE \tag{2.1}$$

where $g(E)$ is normalized to unity [74, 79]. Our plot for specific heat is shown in Fig. 2.6. We have a qualitative agreement with the experiment for our four models while the peak around ($\sim 30K$) is largely affected by the quality of VDOS obtained. Our three models FEAR 216(DZ), FEAR 512(DZ) and FEAR 1024(SZ) provided improvement with respect to experiment [80].

We infer from our calculation of VDOS and specific heat that a larger size model together with a larger basis set gives us a better understanding of these low energy excitations. This further emphasizes the importance of our FEAR method, with the resources available to us it was not possible to fabricate melt-quench models of size 512 and 1024 atoms.

2.4 Conclusions

This chapter presented an investigation pertaining to the complex amorphous material (*a*-Si), which was evaluated with respect to its structural, electronic and vibrational properties. Various model types, MQ and FEAR, were constructed of different sizes for this investigation. Our results revealed that the recently developed FEAR method provides an accurate outcome, which correlates quite well with experimental data, even

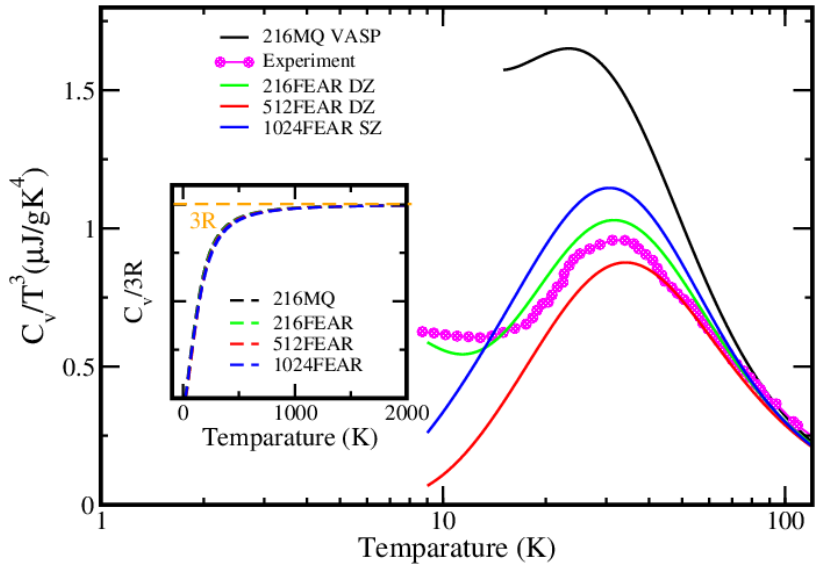

Figure 2.6: Plot of specific-heat (C_v/T^3) for the four models compared with the experimental result [80]. The inset shows the classical (*Dulong-Petit*) limit at higher temperature.

for relatively large structures sizes (512 and 1024). To our knowledge our VDOS result depicts the most clear picture of low energies excitations for *a*-Si. We also obtained a new density for amorphous silicon based on *ab initio* minimum, our result is remarkably close to the experimentally found density.

3 Structure and Dynamics of a Silver-doped Chalcogenide Glass: An *ab initio* Study

The work presented in Chapter 3 has been published in Dale Igram, Horacio E. Castillo, D.A. Drabold, Structure and dynamics of a silver-doped chalcogenide glass: An ab initio study, *Journal of Non-Crystalline Solids*, **514** (2019) 1-9.

3.1 Introduction

When Ag is used to dope Ge_xSe_{1-x} glasses, solid electrolytes, $Ag_y(Ge_xSe_{1-x})_{1-y}$, are created, having very high ionic conductivities [81]. The host network, Ge_xSe_{1-x}, has been broadly investigated for many years experimentally[82–86] and theoretically[87–94]. These studies have revealed that, in general, the $Ge(Se_{1/2})_4$ tetrahedra dominate for $x \leq 0.34$, $Ge(Se_{1/2})_6$ units for $x \geq 0.36$ and $x \leq 0.41$, and orthorhombic (distorted rocksalt) GeSe units for $x \geq 0.42$[95].

Several experimental studies[95–98] have been performed which showed that for Se-rich glasses (i.e. $GeSe_4$) phase separation produced an Ag_2Se glass phase and a Se-deficient matrix, whereas stoichiometric glasses (i.e. $GeSe_2$) contained a $GeSe_2$ glass phase and Ge_2Se_3 glass phase for $y > 0.2$. Ge-rich glasses (i.e. Ge_2Se_3) had a mixture of Ge_2Se_3 and GeSe phases. In a recent publication[99] it was shown that $Ag_y(GeSe_3)_{1-y}$ glasses (for y=0.15 and 0.25) possess insulating and metallic phases with nearly the same energies.

We will present not only the structural, electronic, and Ag ion dynamics, but also, to the best of our knowledge, a first treatment of the vibrational attributes of such systems.

3.2 Methodology

Several methods [15, 100, 101] exist for computational modeling of complex materials. These methods are: empirical potentials, empirical tight-binding methods, and

density functional theory (DFT). Obtaining accurate results for chemically complex systems requires the utilization of an *ab initio* molecular dynamics approach, which incorporates DFT. *ab initio* molecular dynamics (AIMD) allows realistic simulations to be performed without adjustable parameters[102], and is suitable for relatively small systems.

The amorphous $Ag_{0.2}(Ge_{35}Se_{65})_{0.8}$ structure was fabricated using a melt and quench (MQ) approach which utilizes *ab initio* molecular dynamics (AIMD) based on density functional theory (DFT)[103] incorporated in VASP[104–106]. Projected-augmented wave (PAW)[107] pseudo-potentials were used for the description of the core electron-ion interactions and an exchange-correlation functional [108] within the local density approximation (LDA) [109] was considered. The $\Gamma(\vec{k} = 0)$ point was utilized for these calculations along with periodic boundary conditions. The kinetic energy cutoff of the plane-wave varied between 300 and 450 eV with the energy difference criteria being $10^{-4} - 10^{-5}$ eV. A time step of 2 fs was used for the integration of Newton's equations of motion and a constant temperature was achieved by employing the Nose'-Hoover thermostat[110].

3.3 Model

The initial configuration of the $Ag_{0.2}(Ge_{35}Se_{65})_{0.8}$ system consisted of a random-generated structure of 20 Ag atoms, 28 Ge atoms, and 52 Se atoms for a total of 100 atoms. Due to the lack of an experimental atomic density value, an initial guess of 5.0 g/cm^3 with an associated lattice constant of 14.0199Å was considered for the initial cubic simulation cell. The initial guess was obtained from an experimental investigation of a similar MQ structure.

The MQ model was constructed by forming an equilibrated liquid at 2500K for 12 ps, followed by quenching from 2500K to 1500K over 10 ps, then equilibration at 1500K for 6 ps, and quenching from 1500K to 300K within 12 ps and equilibration at 300K for

20 ps. Relaxation at zero pressure was performed which resulted in a triclinic cell having lengths of 13.907Å, 13.334Å and 13.936Å, and a corresponding atomic density of 5.348 g/cm^3. The B/A and C/A ratios for this cell are 0.9568 and 0.9979, respectively. We relaxed the MQ model so the forces were smaller than 0.01 eV/Å. The final structure was then analyzed for the structural, electronic, vibrational, and Ag ion dynamics properties. For the Ag dynamics calculations a temperature of 1000K for 40 ps was used.

3.4 Results and Discussion

3.4.1 Structural Properties

The total and partial pair correlation functions are illustrated in Fig. 3.1. The first and second peaks of the total $g(r)$ correspond to the contributions of AgSe and GeSe, and AgGe, GeGe, and SeSe correlations, respectively. The first peak of g_{GeGe} for 2.52Å≤ r ≤2.67Å is associated with the three Ge-Ge homopolar bonds and the Ge_2Se_3 compounds. The second peak at r= 4.0Å is quite broad and represents the second-nearest neighbors. The distance between Ge atoms of the $Ge(Se_{1/2})_4$ tetrahedra was found to be at r= 4.65Å. The g_{GeSe} correlations within the range of 2.33Å≤ r ≤2.64Å are linked to the Ge_2Se_3 compounds, corner-sharing $Ge(Se_{1/2})_4$ tetrahedra and $GeSe_2$ compounds. Three Se-Se homopolar bonds are represented by the g_{SeSe} correlations for 2.50Å≤ r ≤2.80Å whereas the second-nearest neighbors are located in the range of 3.25Å≤ r ≤4.63Å. There exist g_{AgAg} correlations within the range of 2.62Å≤ r ≤3.48Å. Also, the Ag_2Se compounds have g_{AgSe} correlations in the range of 2.42Å≤ r ≤2.63Å.

Figure 3.2 depicts the static structure factors (total and partials) and reveals that the first sharp diffraction peak (FSDP), a signature of medium range order, is due to the correlations of AgSe and GeSe, which is in contrast to previous studies for other materials that indicate Ge-Ge correlations, located between tetrahedra, are responsible for FSDP[87, 93, 111, 112]. We have produced a rather realistic model for this composition

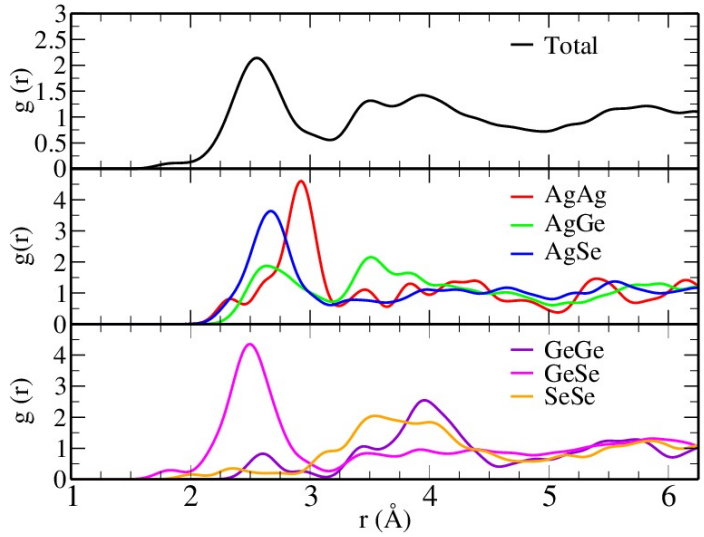

Figure 3.1: Total (top) and partial (center and bottom) pair correlation functions for the $Ag_{20}Ge_{28}Se_{52}$ model.

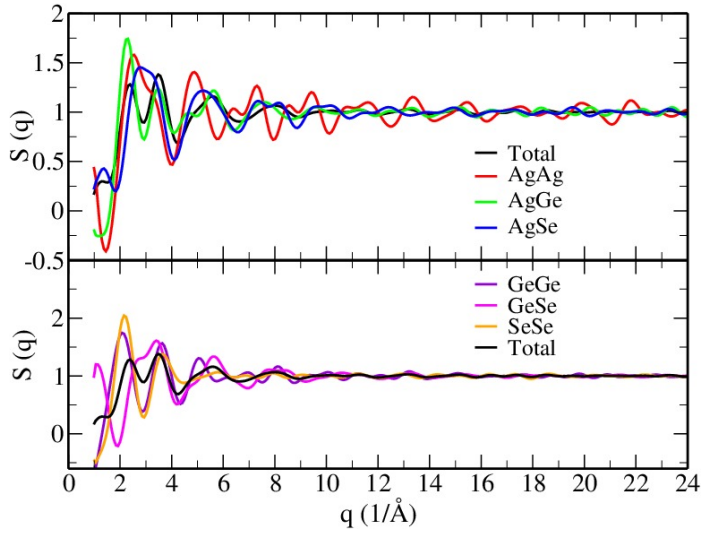

Figure 3.2: Total and partial static structure factors for the $Ag_{20}Ge_{28}Se_{52}$ model.

that will now be the ”simulation benchmark” for future studies of this material. The total structure factor S(q) of our model as compared to the experimental data of Piarristeguy and co-workers[113] is of similar profile and magnitude, but for our model there is a slight

shift to the right for most of the peaks. The experimental value of FSDP is approximately 1.08 $Å^{-1}$, reasonably close to our value of 1.29$Å^{-1}$. This variation is not surprising in part because the experimental results were for a $Ag_{0.2}(GeSe_3)_{0.8}$ system. The first primary peak is basically a result of AgAg, AgGe, GeGe, and SeSe correlations. Both the first and second primary peaks correspond to short-range order (SRO).

A comparison of the radial distribution function (RDF) between the experiment of Fischer-Colbrie et al[114] and our model was performed. The experimental data, shown in Table 3.1, was obtained from a photo-diffused 1500Å film of $Ag_{25}Ge_{25}Se_{50}$ structure with an atomic density of 5.5 g/cm^3, where our model had 5.35 g/cm^3. As reported in [114], the experimental $Ag_{25}Ge_{25}Se_{50}$ structure was prepared in a three-step process: 1) thermal evaporation of 1500Å a-$GeSe_2$ onto a single crystal Si substrate; 2) thermal evaporation of Ag onto a-$GeSe_2$; and 3) exposure to UV light for causing the Ag photo-diffusion. The a-$GeSe_2$ film was created from a source of 99.999%-pure Ge and Se materials, and were degassed, melted together, and homogenized at 800°C for two days. The rates of deposition were 10 Å/s for a-$GeSe_2$ and 1 Å/s for Ag. Operating pressure was less than 10^{-9} Torr. For the UV exposure, an unfiltered 200 W Hg lamp was used as well as a one-hour exposure time for complete Ag diffusion.

Table 3.1: Peak positions for experimental sample ($Ag_{25}Ge_{25}Se_{50}$) and model ($Ag_{20}Ge_{28}Se_{52}$). The peak positions correspond to the three primary peaks and the additional peaks associated with the model are probably due to the small structure size.

Sample	Peak positions (Å)			Additional peaks (Å)	
Experiment (ref. 42)	2.62	3.97	6.15		
Model	2.59	3.99	6.25	3.55	5.87

For comparison, this composition $Ag_{25}Ge_{25}Se_{50}$ is closest to our composition of $Ag_{20}Ge_{28}Se_{52}$. The peak positions for both the model and experimental sample are shown

in Table 3.1. As seen from Table 3.1, three peaks exists experimentally and five for our model. The locations of the first and third peaks of our model are in agreement with the first and second peaks of the experimental results. Our model has an additional two peaks at 3.55Å and 5.87Å, which may be due to small model size.

The total and partial coordination numbers and first peak positions for the glassy phases of Ge_xSe_{1-x} are provided in Table 3.2 for this work, a simulation study[92], and an experimental investigation[115]. According to Table 3.2, Ge is somewhat under-coordinated and Se two-fold coordinated as compared to experiment. The partial coordination numbers indicate, in general, reasonable agreement with experiment, except for Se pairs which is significantly reduced due to bonding with Ag, resulting in other substructures.

Table 3.2: Total and partial coordination numbers and first peak positions for the glassy phases of Ge_xSe_{1-x}. Ref. 14 is a simulation and ref. 43 an experimental study.

Structure	$Ge_{35}Se_{65}$(this work)	$GeSe_2$(ref. 14)	$GeSe_2$(ref. 43)
$n_{GeGe} + n_{GeSe}$	3.75	3.80	4.00
$n_{SeGe} + n_{SeSe}$	1.94	2.08	2.05
n_{GeGe}	0.21	0.25	0.25
n_{GeSe}	3.54	3.55	3.70
n_{SeSe}	0.04	0.30	0.20
r_{GeGe}	2.60	2.44	2.42
r_{GeSe}	1.85	2.36	2.36
r_{SeSe}	2.00	2.37	2.32

The host network ($Ge_{36}Se_{65}$), according to Phillips and Thorpe constraint theory[116–118], has an average coordination number $< n >$ of 2.58 as compared to the 'rigidity percolation threshold' value $< n_p >$ of 2.4 implying that the host network is 'rigid' or 'over-constrained'.

The 100-atom $Ag_{20}Ge_{28}Se_{52}$ model includes corner-shared $Ge(Se_{1/2})_4$ tetrahedra as exemplified by Fig. 3.3. Because the bond angles of these tetrahedra vary significantly (~

90° to 130°) the tetrahedra are quite distorted. As mentioned earlier, this $Ag_{20}Ge_{28}Se_{52}$ model has revealed some interesting substructures, in particular Ag_2Se and Ge_2Se_3, only found in Se-rich and Ge-rich materials, respectively. These substructures are depicted in Fig. 3.4 along with some bond angles.

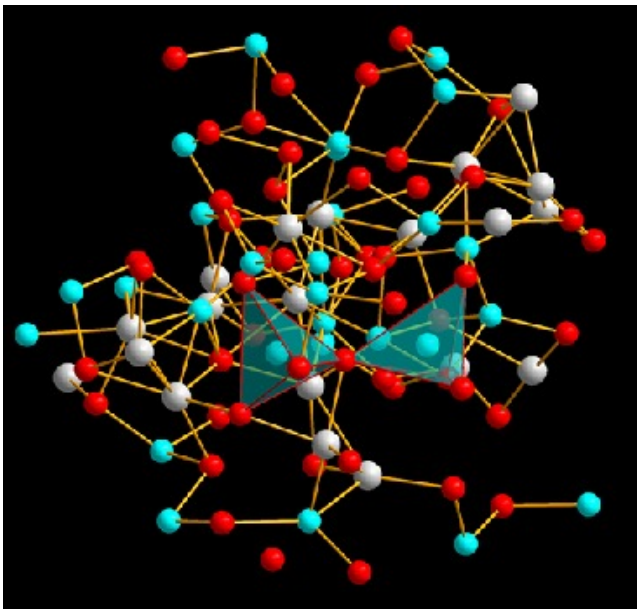

Figure 3.3: An illustration of the two $Ge(Se_{1/2})_4$ units of the $Ag_{20}Ge_{28}Se_{52}$ structure. The Ag, Ge and Se atoms are represented by the color white, blue and red, respectively. The tetrahedra are depicted by the blue shaded regions.

To obtain further insight into the $Ag_{20}Ge_{28}Se_{52}$ structure and its connectivity, ring statistics for each type of atom were computed as illustrated in Fig. 3.5. The 3- and 6-member rings are dominating for Ag and Se, whereas 3-, 4- and 8-member rings dominated for Ge. All three atom types consisted of 10-member rings whereas Se also has 12-member rings. The ring statistics results were obtained by utilizing King's method[29] from the ISAACS software[28].

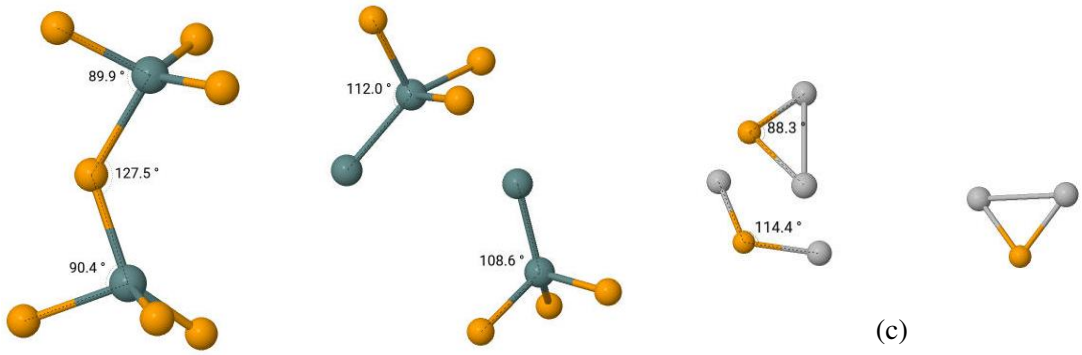

(a) (b) (c)

Figure 3.4: Some substructures that exists in the $Ag_{20}Ge_{28}Se_{52}$ model, (a) a corner-sharing tetrahedra, (b) two Ge_2Se_3, and (c) three Ag_2Se. The green, gold and silver balls represent the Ge, Se and Ag atoms, respectively.

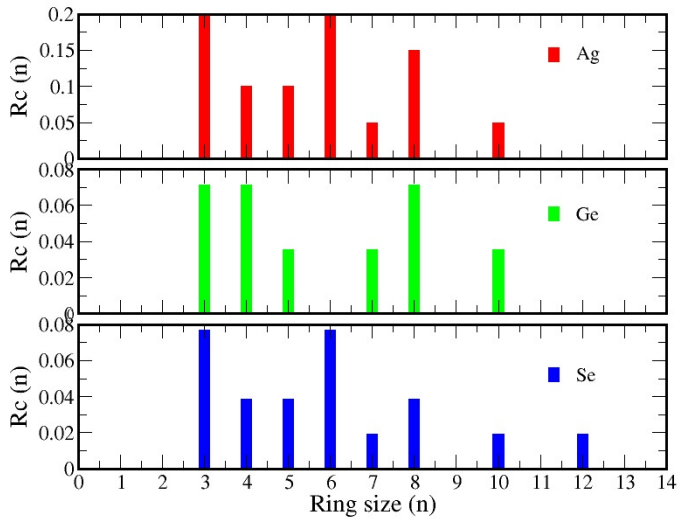

Figure 3.5: Rings per cell (Rc) for the three atomic species. Note: the scale for Ag is more than twice that of Ge and Se.

3.4.2 Electronic Properties

Figure 3.6 reveals the EDOS results for the $Ag_{20}Ge_{28}Se_{52}$ structure. We considered the localization of electronic states by calculating the inverse participation ratio (IPR) given by equation (1.7).

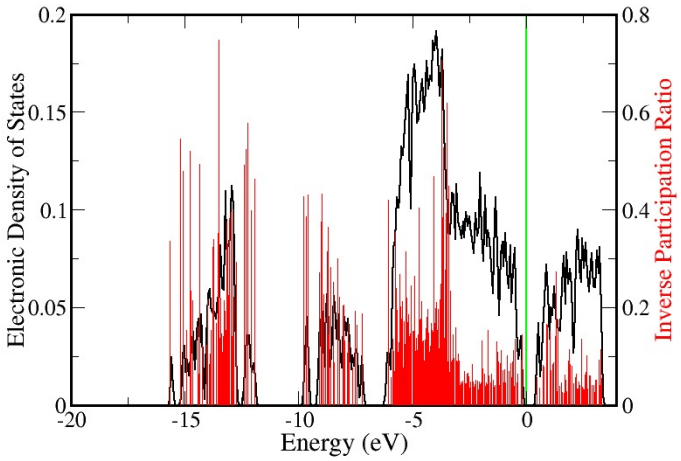

Figure 3.6: Electronic density of states (black line) and Inverse participation ratio (red drop lines) for the $Ag_{20}Ge_{28}Se_{52}$ structure. The Fermi energy is represented by the green line at 0 eV.

As seen in Fig. 3.6, there are extended states near the Fermi level for both the valence and conduction bands in agreement with previous work of Tafen et al.[5]. The LDA energy gap for the Γ-point is approximately 0.40 eV, which is about half of the actual value since it is well known that LDA underestimates the gap energy.

3.4.3 Vibrational Properties

The $Ag_{20}Ge_{28}Se_{52}$ structure can be thought of as two subnetworks (Ag and GeSe host), where the Ag and GeSe subnetworks are weakly and strongly bonded, respectively. It is interesting and novel to understand the dynamics of each subnetwork as well as collectively. One would expect ”soft phonons” for the Ag system, in particular.

Conceptually, there is something akin to an Ag melting transition in which the Ag can hop, but the host is rigid.

A comprehensive understanding of the eigenvectors and eigenvalues of the dynamical matrix enables a detailed analysis of this new composition. The mode analysis consists of the following investigations: i) the degree of mode localization, ii) the amount of bond stretching and bending, iii) mode character (acoustic-like or optical-like), iv) amount of atomic vibrational participation, v) substructure unit vibrations, and vi) tetrahedral breathing A_1 vibration modes of the host network tetrahedra.

The vibrational density of states (VDOS) and inverse participation ratio (VIPR) are both characterized by equations (1.8) and (1.9), respectively. As mentioned in Chapter 1, VIPR quantifies which normal modes are extended or localized.

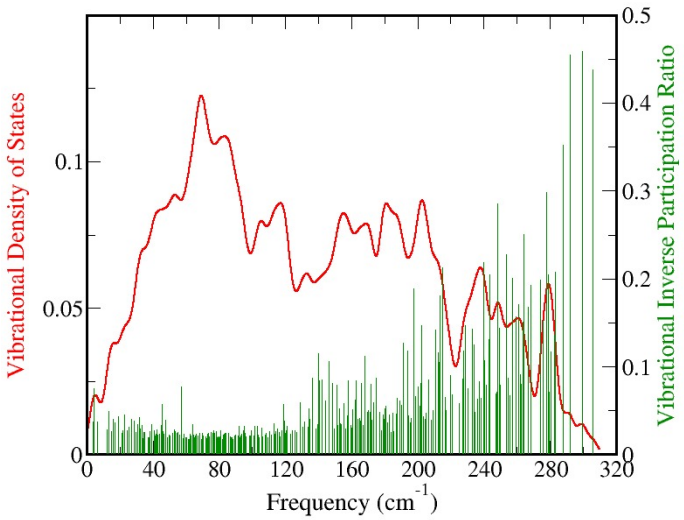

Figure 3.7: Vibrational density of states (red line) and Inverse participation ratio (green drop lines) for the $Ag_{20}Ge_{28}Se_{52}$ structure.

The VDOS and VIPR results, which are presented in Fig. 3.7, indicate extended vibrational states at the low frequencies (0 - 150 cm^{-1}) and more localized states from

approximately 200 - 310 cm^{-1}. When compared to the work done by Cobb and co-workers [87] our VDOS results show the possible influence of the Ag atoms with additional peaks across the vibration spectrum, while our VIPR results having a similar trend with de-localized states at low frequencies and localized ones at higher.

For the total and partial VDOS calculations, Gaussian broadening with a standard deviation sigma value of 3.0 cm^{-1} was employed. As illustrated in Fig. 3.8, the partial VDOS for Se is mostly responsible for the profile and magnitude of the total VDOS which is in reasonable agreement with [87]. Silver makes no contribution beyond approximately 270 cm^{-1}, whereas Ge and Se do.

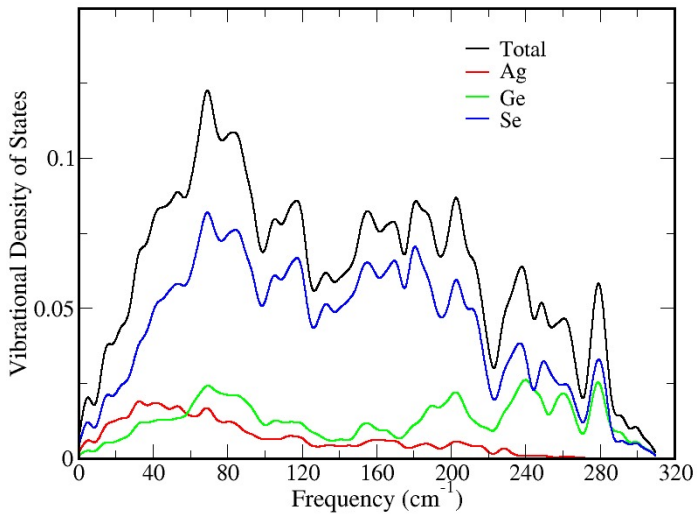

Figure 3.8: Total and partial vibrational density of states for $Ag_{20}Ge_{28}Se_{52}$ structure.

The stretching character quantifies bond stretching or bending as defined by equation (1.10) and illustrated in Fig. 3.9. There are basically three regions of interests: 0-50, 80-160, and 160-310 cm^{-1}. The low-frequency region is mostly of bond-bending character ($S \leq 0.2$) with a small amount of stretching, mid-frequency range has a mixture of bending and stretching characteristics ($0.2 \leq S \leq 0.55$) with the stretching contribution

increasing with frequency, and the high-frequency range having approximately an equal mixture of bending and stretching characters (S≥0.55). An interesting feature is the abrupt change of S that occurs at 160 cm^{-1}, which may be a result of the Ge and Se atoms beginning to increase and decrease their vibrational contribution, respectively, as revealed in Fig. 3.12. The plateau in the high-frequency range is due to the Ge atoms increasing their participation at a higher rate than Se atoms decreasing theirs, and the fact that there are almost twice as many Se atoms as Ge atoms.

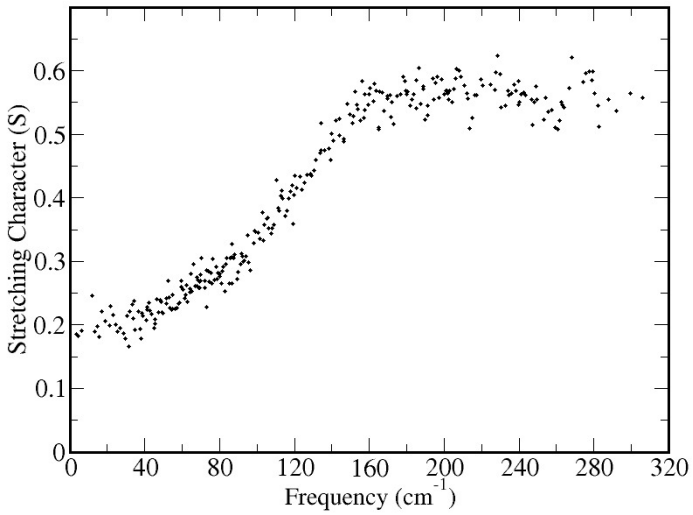

Figure 3.9: Stretching character of the vibrational modes. Note the abrupt change at 160 cm^{-1}.

We calculated the phase quotient q along with its parallel $q_{\|}$ and perpendicular $q_{\perp}$ components as illustrated in Fig. 3.10. All three phase quotients can vary from +1 (acoustic-like modes) to -1 (optical-like modes).

The overall phase quotient q is varying almost linearly from the acoustic-like modes to optical-like modes. The parallel phase quotient $q_{\|}$ exhibits an abrupt change in the range of 100-150 cm^{-1}, whereas the perpendicular phase quotient $q_{\perp}$, in general, is changing linearly in the acoustic-like range until reaching a frequency of 100 cm^{-1} where

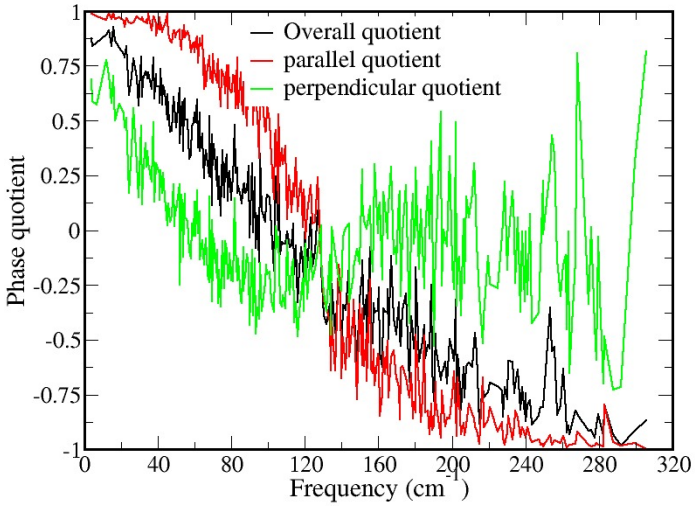

Figure 3.10: Phase quotients of the vibrational modes. The parallel quotient represents the longitudinal modes and perpendicular the traverse modes.

its remains relatively constant to 150 cm^{-1}; thus, exhibiting weak optical-like characteristics. Beyond 150 cm^{-1} there are progressively increasing oscillations of $q_{\perp}$ until reaching a frequency of 300 cm^{-1}. After careful observation of the vibrational behavior of the structure, it appears that this abnormality is due to severe rocking vibrations of a Ge-Ge bond where one of the Ge atoms is bonded to three Se atoms and the other Ge atom to two Ag and Se atoms. This compound is illustrated in Fig. 3.11.

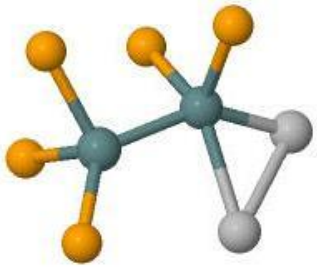

Figure 3.11: Compound responsible for large variations of the perpendicular phase quotient. The color scheme is the same as Fig. 3.4.

Atomic participation ratios[32], as defined by (3.1), were calculated to determine the amount of contribution that each atomic type provided over the vibrational frequency spectrum.

$$P_\alpha(p) = \frac{\sum_{i=1}^{N_\alpha} |u_i^p|}{\sum_{i=1}^{N} |u_i^p|} \tag{3.1}$$

where the numerator is summed over all atoms of atomic type α, the denominator is summed over all atoms in the model, and $\sum_\alpha P_\alpha = 1, \forall\alpha$. As depicted in Fig. 3.12, the Se atoms contribute the most with a peak around 160 cm^{-1}, which is also where the Ge and Ag atoms begin to diverge.

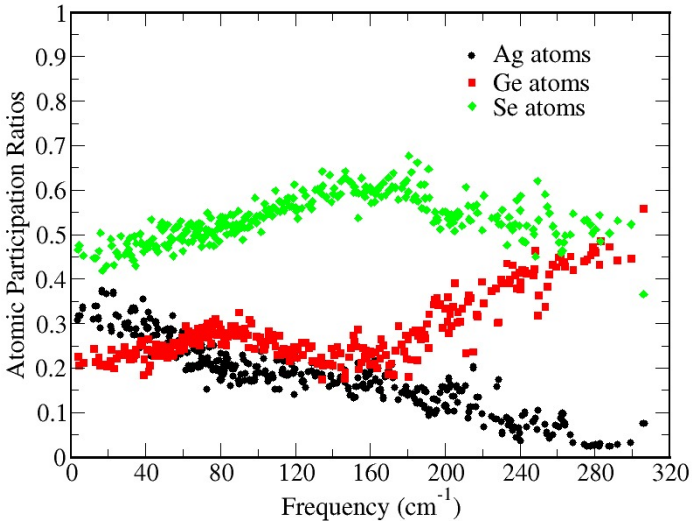

Figure 3.12: Atomic participation ratios for the three atomic species.

Three different types of atomic motion[35] are illustrated in Figs. 3.13 and 3.14. Figure 3.13 represents the three types of atomic motion associated with Ge atoms that are bonded to two Se atoms; whereas, the motions described in Fig. 3.14 are linked to the Se

atoms which are bonded to two Ge atoms. Figures 3.14 and 3.15 reveal that the rocking motion dominates for both Ge and Se atoms, but more for the Se atoms.

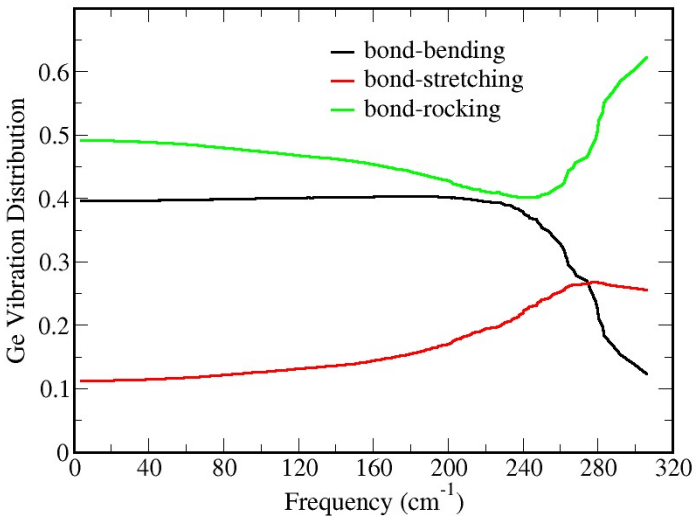

Figure 3.13: Projections of bending, stretching and rocking motions for Ge atoms bonded to two Se atoms.

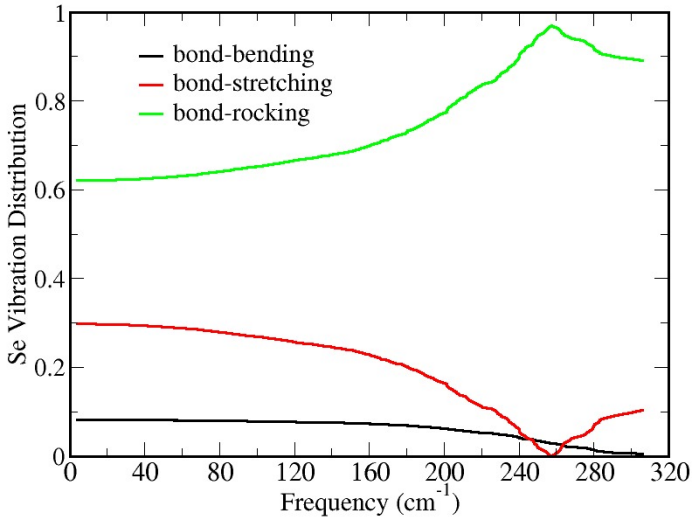

Figure 3.14: Projections of bending, stretching and rocking motions for Se atoms bonded to two Ge atoms.

The host network of the $Ag_{20}Ge_{28}Se_{52}$ model consists of corner-sharing tetrahedra, which exhibits A_1 vibration modes[119, 120]. The A_1 modes (arrows) are illustrated in Fig. 3.15. The quantification of A_1 breathing modes was performed by considering the equation

$$BM(p) = \left| \frac{\sum_{i=1}^{N_b} \hat{u}_i^p \cdot \hat{r}_i}{N_b} \right| \tag{3.2}$$

where i, N_b, $\hat{u}_i^p$, and $\hat{r}_i$ represent neighboring atoms, total number of neighboring atoms, unit displacement and unit distance vector of central atom and neighboring atoms, respectively. The results from equation (11) are shown in Fig. 3.16.

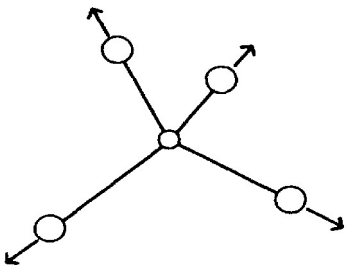

Figure 3.15: A_1 modes of a corner-sharing tetrahedron.

3.4.4 Silver Ion Dynamics

A key property for applications of these materials is the high mobility of silver[121] in a Ge_xSe_{1-x} host network. We computed the mean square displacement (MSD) functions for the three atomic species as depicted in Fig. 3.17. The MSD functions were determined by using

$$\langle r^2(t) \rangle_\alpha = \frac{1}{N_\alpha} \sum_{i=1}^{N_\alpha} \langle |\boldsymbol{r}_i(t) - \boldsymbol{r}_i(0)|^2 \rangle \tag{3.3}$$

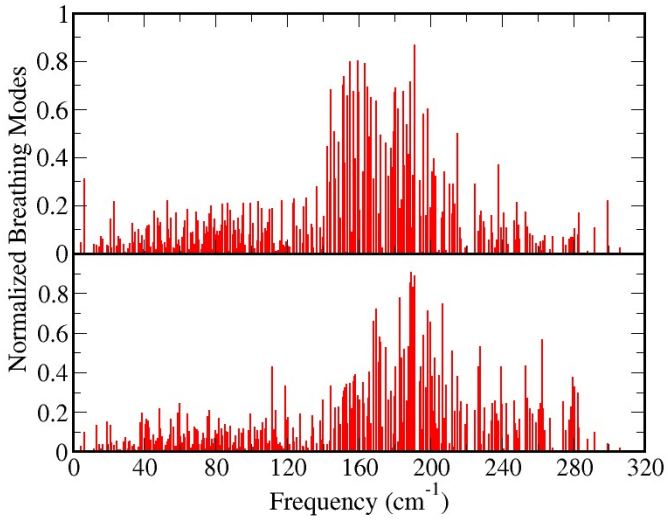

Figure 3.16: Normalized A_1 breathing modes for two corner-sharing $Ge(Se_{1/2})_4$ tetrahedrons utilizing equation (3.11). Two bands of A_1 breathing modes exist having a range of 140 cm^{-1} to 200 cm^{-1} (top panel) and 165 cm^{-1} to 205 cm^{-1} (bottom panel).

where a summed statistical average ($\langle\rangle$) was performed for the three atomic species α. As shown, the MSD of the Ag ions are increasing rapidly with time in contrast to Ge and Se, which implies that Ag ions are more mobile than Ge and Se. The diffusion calculations were performed at a temperature of 1000K. From Fig. 3.17, the self-diffusion coefficient D is calculated using the Einstein relation[122]

$$\langle |\boldsymbol{r}_i(t) - \boldsymbol{r}_i(0)|^2 \rangle = 6Dt + C \tag{3.4}$$

where C represents an integration constant. The conductivity of Ag atoms is calculated using the equation

$$\sigma = \frac{ne^2 D}{k_B T} \tag{3.5}$$

where n is the number density of the Ag atoms. Table 3.3 provides a comparison of the diffusion coefficient and conductivity for the $Ag_{20}Ge_{28}Se_{52}$ model, $Ag_{0.2}(GeSe_3)_{0.8}$

model[7], and $Ag_{0.2}(GeSe_3)_{0.8}$ experimental data [123]. As shown in Table 3.3, the D_{Ag} and σ values are less for the $Ag_{0.2}(Ge_{35}Se_{65})_{0.8}$ model as compared to $Ag_{0.2}(GeSe_3)_{0.8}$ (model) and $Ag_{0.2}(GeSe_3)_{0.8}$ (experimental). This discrepancy may be because of the host network of the $Ag_{0.2}(Ge_{35}Se_{65})_{0.8}$ model is more similar to $GeSe_2$ than $GeSe_3$.

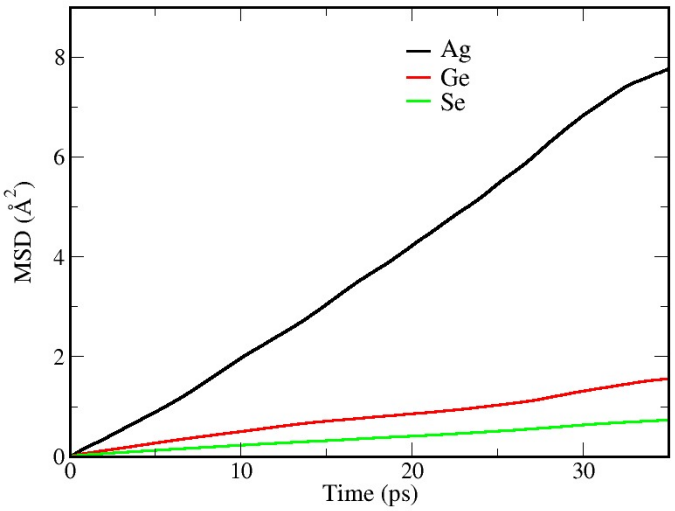

Figure 3.17: Mean square displacement for the three atomic species for the $Ag_{20}Ge_{28}Se_{52}$ structure at T= 1000K.

Table 3.3: Self-diffusion coefficient D and conductivity σ at T=1000K for $Ag_{0.2}(Ge_{35}Se_{65})_{0.8}$, $Ag_{0.2}(GeSe_3)_{0.8}$ (model), and $Ag_{0.2}(GeSe_3)_{0.8}$ (experimental) .

	D_{Ag} (cm^2/s)	σ (S cm^{-1})	*Source*
$Ag_{0.2}(Ge_{35}Se_{65})_{0.8}$	$2.22X10^{-5}$	0.330	This work
$Ag_{0.2}(GeSe_3)_{0.8}$(model)	$2.53X10^{-5}$	0.347	Ref.(23)
$Ag_{0.2}(GeSe_3)_{0.8}$(expt)		0.354	Ref.(57)

We use trajectories of the Ag ions to obtain three-dimensional projections of those trajectories for the most and least mobile Ag atoms in the $Ag_{20}Ge_{28}Se_{52}$ model. Figure

3.18 reveals that the most mobile ion Ag1 has diffused a significant distance in the z direction.

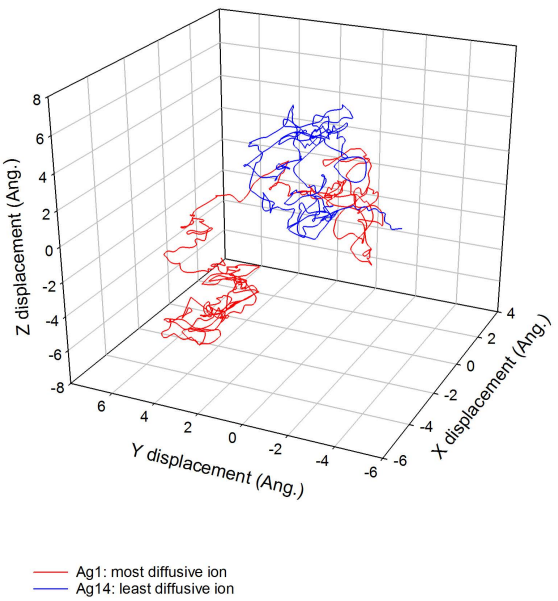

Figure 3.18: Trajectories of the most (red) and least (blue) mobile Ag atoms in $Ag_{20}Ge_{28}Se_{52}$ structure (T=1000K).

As Ag atoms diffuse through a material they can become trapped by their neighboring atoms; thus, affecting the self-diffusion coefficient D and conductivity σ. We have considered the trapping characteristics of the most mobile Ag ion in the $Ag_{20}Ge_{28}Se_{52}$ model. The non-trapping events for this model, illustrated in Fig. 3.19, are represented by abrupt changes in displacement. Possible non-trapping events are highlighted by the shaded regions, which have non-trapping times of approximately 1 to 3ps. These possible events are showing release and capture processes. To accurately determine when a particle is trapped or not is very difficult. At high temperatures the thermal fluctuations would decrease the chances of Ag atoms being trapped resulting in larger diffusion distances.

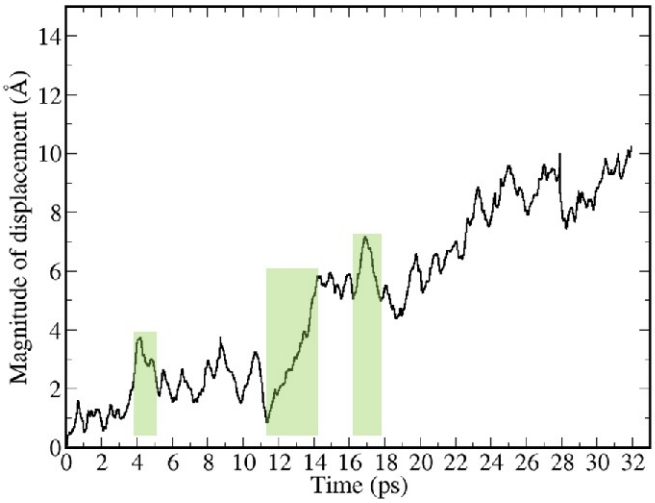

Figure 3.19: Displacement of silver ion A_1 after its initial starting position for T=1000K. The shaded regions depict possible non-trapping events.

The Ag diffusion appears similar to the ”Fluctuating Bond Center Detachment” (FBCD)-assisted diffusion as described by Abtew and coworkers[124].

3.5 Conclusion

Several properties, such as structural, electronic, vibrational, and Ag dynamics were considered for evaluation. Interesting substructures (Ag_2Se, Ge_2Se_3) were revealed, which are commonly associated with Se-rich or Ge-rich systems. Our model showed a FSDP for a high Ag concentration in agreement with other published results, but was due to correlations of AgSe and GeSe, not from GeGe correlations as is typically reported. We revealed that the radial distribution function of our model yielded fairly good agreement with experiment. We believe that this is a first attempt to provide a detailed analysis of the vibrational modes for a AgGeSe system. Both the vibrational density of states and atomic participation ratios calculations revealed that Se atoms are a major contributor across the vibrational spectrum. The abrupt change and plateau of the stretching character may be due to vibrational contribution changes and a difference in the rate of change for the Ge

and Se atoms, respectively. We learned that the divergence of the perpendicular phase quotient is due to the rocking motion of a Ge-Ge compound. We investigated A_1 breathing modes of the corner-sharing tetrahedra which revealed that these breathing modes are non-local and involve the mixing of modes of different symmetry resulting in two bands of A_1 breathing modes. Despite the existence of some interesting substructures the self-diffusion coefficient and conductivity values were reasonably close to published results. Trapping and release processes associated with the most diffusing Ag ion were briefly discussed.

4 Conclusion and Future Work

This dissertation considered two different materials for investigation. These were a non-glass former (*a*-Si) and a glass former ($Ag_{0.2}(Ge_{35}Se_{65})_{0.8}$). Several physical, electrical, and dynamical attributes of these materials were evaluated, which revealed new insight into our understanding of the behavior for these materials with regards to various applications.

4.1 Conclusion

An investigation pertaining to the complex amorphous material (*a*-Si) was performed with respect to its structural, electronic and vibrational properties. This investigation consisted of several model types of different sizes which were constructed from the MQ and FEAR methods. Models with less than 512 atoms were shown to be inadequate in resolving the first peak in $S(Q)$ for low Q, whereas the 1024 FEAR model was as good as the much larger models. The electronic density of states for four models (216MQ, 216FEAR, 512FEAR, 1024FEAR) bear qualitative similarity, with some localized states located near the Fermi energy, due to defects, for the larger models. The vibrational calculations revealed that a double-zeta basis is required to obtain a satisfactory vibrational spectrum. It was shown that the recently developed FEAR method provides models, which correlates quite well with experimental data, even for relatively large structures sizes, and with substantial efficiency improvements relative to standard methods. Our VDOS result illustrates a much clearer picture of low energy excitations for *a*-Si. A new density of amorphous silicon established by *ab initio* minimum was determined to be extremely close to the experimental density.

The evaluation of several static and dynamic properties of an amorphous $Ag_{0.2}(Ge_{35}Se_{65})_{0.8}$ model was presented. Our static structure factor results revealed a FSDP for a high Ag content which agreed with other published work, which was not due

to GeGe correlations as reported in other materials, but instead due to AgSe and GeSe correlations. We revealed that the radial distribution function of our model yielded fairly good agreement with experiment. The host network ($Ge_{36}Se_{65}$), which consists of three and four-fold Ge atoms and two-fold Se atoms, has been found to be a rigid network, in accord with simple coordination models of network rigidity. In addition, the model also contains $Ge(Se_{1/2})_4$ tetrahedra that have been shown to be very distorted. It was determined that the partial coordination numbers, in general, agreed with experiment except for Se pairs which was decreased significantly due to bonding with Ag, producing other substructures (Ag_2Se, Ge_2Se_3). We believe that this is a first detailed calculation of the vibrational modes for a AgGeSe system. The VIPR results indicated that extended vibrational states were located at the low frequencies and more localized states at higher ones. When compared to previous work, the VDOS results illustrated additional peaks which may be due to the influence of the Ag atoms. From both the partial VDOS and atomic participation ratio calculations it was shown that Se atoms are a major contributor across the vibrational spectrum. The stretching character increased rapidly around 160 cm^{-1} and a plateau, which is believed to be the result of vibrational contribution changes and a difference in the rate of these vibrational changes for the Ge and Se atoms, respectively. It was concluded, from careful observations, that the large variations of the perpendicular phase quotient was due to the rocking motion of a Ge-Ge compound as a result of an atomic weight imbalance of the Ge-Ge compound. Projections of the bending, stretching, and rocking motions revealed that the rocking motion manifested for both Ge and Se atoms, but more for the Se atoms. We investigated A_1 breathing modes of the corner-sharing tetrahedra which revealed that these breathing modes are non-local and involve the mixing of modes for different symmetry resulting in two bands of A_1 breathing modes. Despite the existence of some interesting substructures the self-diffusion coefficient and conductivity values were reasonably close to published results. The Ag ion

study regarding the trapping and release processes for the most mobile Ag ion revealed ”diffusion” times of about 1 to 3 ps, which would increase as temperature increased.

4.2 Future Work

With regards to amorphous silicon, it would be interesting to contrast the results of a FEAR model with size of 2048 atoms using a double zeta basis set with the results presented in Chapter 2, just to see how much of an improvement in the results would occur and in what areas. For the amorphous silver-doped chalcogenide glass, it may be worth performing a similar study as was done in Chapter 3, but with a larger model (> 100 atoms) produced by the FEAR method and consisting of a $GeSe_2$ host network. Results from the larger model and Chapter 3 can be compared to determine any improvement as well as the robustness of the FEAR algorithm. In addition, obtaining detailed analysis of electrical conductivity on these systems may reveal interesting and unexplained conductivity fluctuations in time.

References

[1] J. Singh and K. Shimakawa, *Advances in amorphous semiconductors*. CRC Press, 2003.

[2] S. R. Elliott, "Physics of amorphous materials," *Longman Group, Longman House, Burnt Mill, Harlow, Essex CM 20 2 JE, England, 1983.*, 1983.

[3] M. Kostyshin, E. Mikhailovskaya, and P. Romanenko, "On the effect on photosensitivity of thin semiconductor layers on metallic substrates," *Fiz. Tverd. Tela*, vol. 8, no. 2, pp. 571–572, 1966.

[4] M. Frumar and T. Wagner, "Ag doped chalcogenide glasses and their applications," *Current opinion in solid state and materials science*, vol. 7, no. 2, pp. 117–126, 2003.

[5] D. Drabold, M. Mitkova, *et al.*, "Silver transport in GexSe1- x:Ag materials: Ab initio simulation of a solid electrolyte," *Physical Review B*, vol. 72, no. 5, p. 054206, 2005.

[6] I. Chaudhuri, F. Inam, and D. Drabold, "Ab initio determination of ion traps and the dynamics of silver in silver-doped chalcogenide glass," *Physical Review B*, vol. 79, no. 10, p. 100201, 2009.

[7] B. Prasai and D. Drabold, "Ab initio simulation of solid electrolyte materials in liquid and glassy phases," *Physical Review B*, vol. 83, no. 9, p. 094202, 2011.

[8] A. Piarristeguy, G. Cuello, A. Fernández-Martínez, V. Cristiglio, M. Johnson, M. Ribes, and A. Pradel, "Short range order and Ag diffusion threshold in Agx(Ge0.25Se0.75)100- x glasses," *physica status solidi (b)*, vol. 249, no. 10, pp. 2028–2033, 2012.

[9] R. M. Martin, *Electronic structure: basic theory and practical methods*. Cambridge university press, 2004.

[10] A. V. Kolobov and J. Tominaga, *Chalcogenides: metastability and phase change phenomena*, vol. 164. Springer Science & Business Media, 2012.

[11] J. P. Perdew and Y. Wang, "Accurate and simple analytic representation of the electron-gas correlation energy," *Physical Review B*, vol. 45, no. 23, p. 13244, 1992.

[12] J. P. Perdew, K. Burke, and M. Ernzerhof, "Generalized gradient approximation made simple," *Physical review letters*, vol. 77, no. 18, p. 3865, 1996.

[13] K. Laasonen, R. Car, C. Lee, and D. Vanderbilt, "Implementation of ultrasoft pseudopotentials in ab initio molecular dynamics," *Physical Review B*, vol. 43, no. 8, p. 6796, 1991.

[14] G. Kresse and D. Joubert, "From ultrasoft pseudopotentials to the projector augmented-wave method," *Physical Review B*, vol. 59, no. 3, p. 1758, 1999.

[15] W. Kohn and L. J. Sham, "Self-consistent equations including exchange and correlation effects," *Physical review*, vol. 140, no. 4A, p. A1133, 1965.

[16] E. R. Davidson and W. J. Thompson, "Monster matrices: their eigenvalues and eigenvectors," *Computers in Physics*, vol. 7, no. 5, pp. 519–522, 1993.

[17] J. M. Soler, E. Artacho, J. D. Gale, A. García, J. Junquera, P. Ordejón, and D. Sánchez-Portal, "The siesta method for ab initio order-n materials simulation," *Journal of Physics: Condensed Matter*, vol. 14, no. 11, p. 2745, 2002.

[18] N. Metropolis, A. W. Rosenbluth, M. N. Rosenbluth, A. H. Teller, and E. Teller, "Equation of state calculations by fast computing machines," *The journal of chemical physics*, vol. 21, no. 6, pp. 1087–1092, 1953.

[19] R. McGreevy and L. Pusztai, "Reverse monte carlo simulation: a new technique for the determination of disordered structures," *Molecular simulation*, vol. 1, no. 6, pp. 359–367, 1988.

[20] R. L. McGreevy, "Reverse monte carlo modelling," *Journal of Physics: Condensed Matter*, vol. 13, no. 46, p. R877, 2001.

[21] P. Biswas, D. N. Tafen, and D. A. Drabold, "Experimentally constrained molecular relaxation: The case of glassy $Gese_2$," *Phys. Rev. B*, vol. 71, p. 054204, 2005.

[22] O. Gereben and L. Pusztai, "Rmc_pot: a computer code for reverse monte carlo modeling the structure of disordered systems containing molecules of arbitrary complexity," *Journal of computational chemistry*, vol. 33, no. 29, pp. 2285–2291, 2012.

[23] G. Opletal, T. Petersen, D. McCulloch, I. Snook, and I. Yarovsky, "The structure of disordered carbon solids studied using a hybrid reverse monte carlo algorithm," *Journal of Physics: Condensed Matter*, vol. 17, no. 17, p. 2605, 2005.

[24] M. J. Cliffe, M. T. Dove, D. Drabold, and A. L. Goodwin, "Structure determination of disordered materials from diffraction data," *Physical review letters*, vol. 104, no. 12, p. 125501, 2010.

[25] Y. Youn, Y. Kang, and S. Han, "An efficient method to generate amorphous structures based on local geometry," *Computational Materials Science*, vol. 95, pp. 256–262, 2014.

[26] A. Pandey, P. Biswas, and D. A. Drabold, "Force-enhanced atomic refinement: Structural modeling with interatomic forces in a reverse mont carlo approach applied to amorphous si and sio2," *Phys.Rev.B*, vol. 92, p. 155205, 2015.

[27] T. Egami and S. J. Billinge, *Underneath the Bragg peaks: structural analysis of complex materials*, vol. 16. Newnes, 2012.

[28] S. Le Roux and P. Jund, "Ring statistics analysis of topological networks: New approach and application to amorphous GeS2 and SiO2 systems," *Computational Materials Science*, vol. 49, no. 1, pp. 70–83, 2010.

[29] S. V. King, "Ring configurations in a random network model of vitreous silica," *Nature*, vol. 213, no. 5081, p. 1112, 1967.

[30] K. Morigaki and C. Ogihara, "Amorphous semiconductors: Structure, optical, and electrical properties," in *Springer Handbook of Electronic and Photonic Materials*, pp. 1–1, Springer, 2017.

[31] S. Taraskin and S. Elliott, "Nature of vibrational excitations in vitreous silica," *Physical Review B*, vol. 56, no. 14, p. 8605, 1997.

[32] N. Zotov, I. Ebbsjö, D. Timpel, and H. Keppler, "Calculation of Raman spectra and vibrational properties of silicate glasses: comparison between Na2Si4O9 and SiO2 glasses," *Physical Review B*, vol. 60, no. 9, p. 6383, 1999.

[33] B. Bhattarai and D. Drabold, "Vibrations in amorphous silica," *Journal of Non-Crystalline Solids*, vol. 439, pp. 6–14, 2016.

[34] R. Bell and D. Hibbins-Butler, "Acoustic and optical modes in vitreous silica, germania and beryllium fluoride," *J. Phys. C: Solid State Phys.*, vol. 8, p. 787, 1975.

[35] R. Bell, P. Dean, and D. Hibbins-Butler, "Normal mode assignments in vitreous silica, germania and beryllium fluoride," *Journal of Physics C: Solid State Physics*, vol. 4, no. 10, p. 1214, 1971.

[36] R. A. Street, ed., vol. 37. Singapore: Springer-Verlag Berlin Heidelberg, 2000.

[37] B. Djordjevic, M. Thorpe, and F. Wooten, "Computer model of tetrahedral amorphous diamond," *Phys.Rev.B*, vol. 52, pp. 5685–5689, 1995.

[38] F. Wooten, K. Winer, and D. Weaire, "Computer generation of structural models of amorphous si and ge," *Phys.Rev.Lett.*, vol. 54, pp. 1392–1395, 1985.

[39] G. T. Barkema and N. Mousseau, "Event-based relaxation of continuous disordered systems," *Phys. Rev. Lett.*, vol. 77, pp. 4358–4361, 1996.

[40] N. Mousseau and G. T. Barkema, "Activated mechanisms in amorphous silicon: An activation-relaxation-technique study," *Phys. Rev. B*, vol. 61, pp. 1898–1906, 2000.

[41] D. A. Drabold, "Topics in the theory of amorphous materials," *Eur.Phys.J. B*, vol. 68, pp. 1–21, 2009.

[42] J. Tersoff, "Empirical interatomic potential for carbon, with applications to amorphous carbon," *Phys. Rev. Lett.*, vol. 61, pp. 2879–2882, 1988.

[43] N. A. Marks, "Generalizing the environment-dependent interaction potential for carbon," *Phys.Rev.B*, vol. 63, p. 035401, 2000.

[44] R. Car and M. Parrinello, "Structural, dynamical, and electronic properties of amorphous silicon: An ab initio molecular-dynamics study," *Phys. Rev. Lett.*, vol. 60, pp. 204–207, Jan 1988.

[45] D. A. Drabold, P. A. Fedders, O. F. Sankey, and J. D. Dow, "Molecular-dynamics simulations of amorphous si," *Phys. Rev. B*, vol. 42, pp. 5135–5141, Sep 1990.

[46] N. Cooper, C. Goringe, and D. McKenzie, "Density functional theory modelling of amorphous silicon," *Computational Materials Science*, vol. 17, no. 1, pp. 1 – 6, 2000.

[47] R. L. McGreevy and L. Pusztai, "Reverse monte carlo simulation: a new technique for the determination of disordered structures," *Mol. Simul.*, vol. 1, pp. 359–367, 1988.

[48] R. L. McGreevy, "Reverse monte carlo modelling," *Journal of Physics: Condensed Matter*, vol. 13, no. 46, p. R877, 2001.

[49] D. Keen and R. L. McGreevy, "Structural modelling of glasses using reverse monte carlo simulation," *Nature*, vol. 344, pp. 423–425, 1990.

[50] P. Biswas, R. Atta-Fynn, and D. A. Drabold, "Reverse monte carlo modeling of amorphous silicon," *Phys. Rev. B*, vol. 69, p. 195207, 2004.

[51] G. Opletal, T. C. Petersen, A. S. Barnard, and S. P. Russo, "On reverse monte carlo constraints and model reproduction," *J. Comput. Chem.*, vol. 38, pp. 1547–1551, 2017.

[52] M. J. Cliffe, A. P. Bartok, R. N. Kerber, C. P. Grey, G. Csanyi, and A. L. Goodwin, "Structural simplicity as a restraint on the structure of amorphous silicon," *Phys.Rev.B*, vol. 95, pp. 224108(1–6), 2017.

[53] P. Biswas, R. Atta-Fynn, and D. A. Drabold, "Experimentally constrained molecular relaxation: The case of hydrogenated amorphous silicon," *Phys. Rev. B*, vol. 76, p. 125210, 2007.

[54] B. Meredig and C. Wolverton, "A hybrid computational–experimental approach for automated crystal structure solution," *Nature Materials*, vol. 12, p. 123 EP, 11 2012.

[55] A. Pandey, P. Biswas, and D. A. Drabold, "Inversion of diffraction data for amorphous materials," *Scientific Reports*, vol. 6, p. 33731, 2016.

[56] A. Pandey, P. Biswas, B. Bhattarai, and D. A. Drabold, "Realistic inversion of diffraction data for an amorphous solid: The case of amorphous silicon," *Phys.Rev.B*, vol. 94, p. 235208, 2016.

[57] B. Bhattarai, A. Pandey, and D. Drabold, "Evolution of amorphous carbon across densities: An inferential study," *Carbon*, pp. –, 2018.

[58] M. G. Tucker, D. A. Keen, M. T. Dove, A. L. Goodwin, and Q. Hui, "Rmcprofile: reverse monte carlo for polycrystalline materials," *J. Phys.: Condens. Matter*, vol. 19, p. 335218, 2007.

[59] J. M. Soler, E. Artacho, J. D. Gale, A. Garca, J. Junquera, P. Ordejon, and D. Sanchez-Portal, "The siesta method for ab initio order-n materials simulation," *Journal of Physics: Condensed Matter*, vol. 14, pp. 2745–2779, 2002.

[60] G. Kresse and J. Furthmuller, "Efficient iterative schemes for ab initio total-energy calculations using a plane-wave basis set," *Phys.Rev.B*, vol. 54, pp. 11169–11186, 1996.

[61] M. Hacene, A. Anciaux-Sedrakian, X. Rozanska, D. Klahr, T. Guignon, and P. Fleurat-Lessard, "Accelerating vasp electronic structure calculations using graphic processing units," *Journal of Computational Chemistry*, vol. 33, no. 32, pp. 2581–2589, 2012.

[62] M. Hutchinson and M. Widom, "Vasp on a gpu: Application to exact-exchange calculations of the stability of elemental boron," *Computer Physics Communications*, vol. 183, no. 7, pp. 1422 – 1426, 2012.

[63] K. Laaziri, S. Kycia, S. Roorda, M. Chicoine, J. L. Robertson, J. Wang, and S. C. Moss, "High resolution radial distribution function of pure amorphous silicon," *Phys. Rev. Lett.*, vol. 82, pp. 3460–3463, 1999.

[64] V. L. Deringer, N. Bernstein, A. P. Bartok, M. J. Cliffe, R. N. Kerber, L. E. Marbella, C. P. Grey, S. R. Elliott, and G. Csanyi, "Realistic atomistic structure of amorphous silicon from machine-learning-driven molecular dynamics," *arXiv:1803.02802*, 2018.

[65] K. Jarolimek, R. A. de Groot, G. A. de Wijs, and M. Zeman, "First-principles study of hydrogenated amorphous silicon," *Phys. Rev. B*, vol. 79, p. 155206, 2009.

[66] R. Atta-Fynn and P. Biswas, "Nearly defect-free dynamical models of disordered solids: The case of amorphous silicon," *arXiv:1803.05133*, 2018.

[67] J. Fortner and J. S. Lannin, "Radial distribution functions of amorphous silicon," *Phys. Rev. B*, vol. 39, pp. 5527–5530, Mar 1989.

[68] G. Opletal, T. Petersen, B. Omalley, I. Snook, D. G. Mcculloch, N. A. Marks, and I. Yarovsky, "Hybrid approach for generating realistic amorphous carbon structure using metropolis and reverse monte carlo," *Mol. Sim.*, vol. 28, pp. 927–938, 2002.

[69] S. King *Nature*, vol. 213, p. 1112, 1967.

[70] S. Roux and V. Petkov, "Isaacs interactive structure analysis of amorphous and crystalline systems," *J. Appl. Cryst.*, vol. 43, pp. 181–185, 2010.

[71] K. Prasai, P. Biswas, and D. A. Drabold, "Electronically designed amorphous carbon and silicon," *Phys. Status Solidi A*, vol. 213, pp. 1653–1660, 2016.

[72] J. H. Los and T. D. Kühne, "Inverse simulated annealing for the determination of amorphous structures," *Phys. Rev. B*, vol. 87, p. 214202, 2013.

[73] G. P. Lopinski, V. I. Merkulov, and J. S. Lanin, "Vibrational states of tetrahedral amorphous carbon," *Appl. Phys. Lett.*, vol. 69, pp. 3348–3350, 1996.

[74] B. Bhattarai and D. A. Drabold, "Amorphous carbon at low densities: An ab initio study," *Carbon*, vol. 115, pp. 532–538, 2017.

[75] B. Bhattarai and D. A. Drabold, "Vibrations in amorphous silica," *Journal of Non-Crystalline Solids*, vol. 439, pp. 6–14, 2016.

[76] W. A. Kamitakahara, C. M. Soukoulis, H. R. Shanks, U. Buchenau, and G. S. Grest, "Vibrational spectrum of amorphous silicon: Experiment and computer simulation," *Phys. Rev. B*, vol. 36, pp. 6539–6542, Oct 1987.

[77] J. S. Custer, M. O. Thompson, D. C. Jacobson, J. M. Poate, S. Roorda, W. C. Sinke, and F. Spaepen, "Density of amorphous si," *Applied Physics Letters*, vol. 64, no. 4, pp. 437–439, 1994.

[78] A. Maradudin, E. Montroll, and G. H. Weiss, *Theory of Lattice Dyanmics in the Harmonic Approximation*, p. 123. Newyork: Academic Press, 1963.

[79] S. M. Nakhmanson and D. A. Drabold, "Low-temperature anomalous specific heat without tunneling modes: A simulation for $a-$ Si with voids," *Phys. Rev. B*, vol. 61, pp. 5376–5380, 2000.

[80] B. L. Zink, R. Pietri, and F. Hellman, "Thermal conductivity and specific heat of thin-film amorphous silicon," *Phys. Rev. Lett.*, vol. 96, p. 055902, 2006.

[81] M. Kobayashi, "Review on structural and dynamical properties of silver chalcogenides," *Solid State Ionics*, vol. 39, no. 3-4, pp. 121–149, 1990.

[82] P. Boolchand, J. Grothaus, W. Bresser, and P. Suranyi, "Structural origin of broken chemical order in a GeSe2 glass," *Physical Review B*, vol. 25, no. 4, p. 2975, 1982.

[83] P. S. Salmon, "Structure of liquids and glasses in the Ge–Se binary system," *Journal of Non-Crystalline Solids*, vol. 353, no. 32-40, pp. 2959–2974, 2007.

[84] S. Bhosle, K. Gunasekera, P. Chen, P. Boolchand, M. Micoulaut, and C. Massobrio, "Meeting experimental challenges to physics of network glasses: Assessing the role of sample homogeneity," *Solid State Communications*, vol. 151, no. 24, pp. 1851–1855, 2011.

[85] K. Gunasekera, S. Bhosle, P. Boolchand, and M. Micoulaut, "Superstrong nature of covalently bonded glass-forming liquids at select compositions," *The Journal of chemical physics*, vol. 139, no. 16, p. 164511, 2013.

[86] P. Boolchand, M. Bauchy, M. Micoulaut, and C. Yildirim, "Topological phases of chalcogenide glasses encoded in the melt dynamics," *physica status solidi (b)*, 2018.

[87] M. Cobb, D. Drabold, and R. Cappelletti, "Ab initio molecular-dynamics study of the structural, vibrational, and electronic properties of glassy GeSe2," *Physical Review B*, vol. 54, no. 17, p. 12162, 1996.

[88] X. Zhang and D. Drabold, "Structural and electronic properties of glassy GeSe2 surfaces," *Physical Review B*, vol. 62, no. 23, p. 15695, 2000.

[89] D. Drabold *et al.*, "Models and modeling schemes for binary IV-VI glasses," *Physical Review B*, vol. 71, no. 5, p. 054206, 2005.

[90] M. Micoulaut, R. Vuilleumier, and C. Massobrio, "Improved modeling of liquid GeSe2: impact of the exchange-correlation functional," *Physical Review B*, vol. 79, no. 21, p. 214205, 2009.

[91] S. Le Roux, A. Bouzid, M. Boero, and C. Massobrio, "Structural properties of glassy Ge2Se3 from first-principles molecular dynamics," *Physical Review B*, vol. 86, no. 22, p. 224201, 2012.

[92] M. Micoulaut, A. Kachmar, M. Bauchy, S. Le Roux, C. Massobrio, and M. Boero, "Structure, topology, rings, and vibrational and electronic properties of Gex Se1-x glasses across the rigidity transition: a numerical study," *Physical Review B*, vol. 88, no. 5, p. 054203, 2013.

[93] M. T. Shatnawi, "Reverse Monte Carlo Modeling of the Rigidity Percolation Threshold in GexSe1-x Glassy Networks," *New Journal of Glass and Ceramics*, vol. 5, no. 03, p. 31, 2015.

[94] S. Le Roux, A. Bouzid, K. Y. Kim, S. Han, A. Zeidler, P. S. Salmon, and C. Massobrio, "Structure of amorphous GeSe9 by neutron diffraction and first-principles molecular dynamics: Impact of trajectory sampling and size effects," *The Journal of chemical physics*, vol. 145, no. 8, p. 084502, 2016.

[95] M. Mitkova, Y. Wang, and P. Boolchand, "Dual chemical role of Ag as an additive in chalcogenide glasses," *Physical Review Letters*, vol. 83, no. 19, p. 3848, 1999.

[96] Y. Wang, M. Mitkova, D. Georgiev, S. Mamedov, and P. Boolchand, "Macroscopic phase separation of Se-rich (x¡ 1/3) ternary Agy(GexSe1- x)1- y glasses," *Journal of Physics: Condensed Matter*, vol. 15, no. 16, p. S1573, 2003.

[97] E. Bychkov, V. Tsegelnik, Y. Vlasov, A. Pradel, and M. Ribes, "Percolation transition in Ag-doped germanium chalcogenide-based glasses: conductivity and silver diffusion results," *Journal of non-crystalline solids*, vol. 208, no. 1-2, pp. 1–20, 1996.

[98] M. Mitkova and M. Kozicki, "Silver incorporation in Ge–Se glasses used in programmable metallization cell devices," *Journal of non-crystalline solids*, vol. 299, pp. 1023–1027, 2002.

[99] K. Prasai, G. Chen, and D. Drabold, "Amorphous to amorphous insulator-metal transition in GeSe3:Ag glasses," *Physical Review Materials*, vol. 1, no. 1, p. 015603, 2017.

[100] M. Cohen and V. Heine, "Solid state physics vol 24 ed f seitz," *D Turnbull and H Ehrenreich (New York: Academic) pp*, pp. 37–248, 1970.

[101] W. A. Harrison, *Electronic structure and the properties of solids: the physics of the chemical bond*. Courier Corporation, 2012.

[102] R. Iftimie, P. Minary, and M. E. Tuckerman, "Ab initio molecular dynamics: Concepts, recent developments, and future trends," *Proceedings of the National Academy of Sciences*, vol. 102, no. 19, pp. 6654–6659, 2005.

[103] T. Ziegler, "Approximate density functional theory as a practical tool in molecular energetics and dynamics," *Chemical Reviews*, vol. 91, no. 5, pp. 651–667, 1991.

[104] G. Kresse, "A computer simulation of nucleation and growth of thin films," *Comput. Mater. Sci.*, vol. 6, p. 15, 1996.

[105] G. Kresse, "Efficient iterative schemes for ab initio total-energy calculations using a plane-wave basis set," *Phys. Rev. B*, vol. 54, p. 11169, 1996.

[106] M. Hacene, A. Anciaux-Sedrakian, X. Rozanska, D. Klahr, T. Guignon, and P. Fleurat-Lessard, "Accelerating VASP electronic structure calculations using graphic processing units," *Journal of computational chemistry*, vol. 33, no. 32, pp. 2581–2589, 2012.

[107] G. Kresse, "From ultrasoft pseudopotentials to the projector augmented-wave method," *Phys. Rev. B*, vol. 59, p. 1758, 1999.

[108] D. N. Laikov, "Fast evaluation of density functional exchange-correlation terms using the expansion of the electron density in auxiliary basis sets," 1997.

[109] P. Hohenberg and W. Kohn, "Inhomogeneous electron gas," *Physical review*, vol. 136, no. 3B, p. B864, 1964.

[110] S. Nosé, "A molecular dynamics method for simulations in the canonical ensemble," *Molecular physics*, vol. 52, no. 2, pp. 255–268, 1984.

[111] H. Iyetomi, P. Vashishta, and R. K. Kalia, "Incipient phase separation in Ag/Ge/Se glasses: clustering of Ag atoms," *Journal of non-crystalline solids*, vol. 262, no. 1-3, pp. 135–142, 2000.

[112] S. Elliott, "Origin of the first sharp diffraction peak in the structure factor of covalent glasses," *Physical review letters*, vol. 67, no. 6, p. 711, 1991.

[113] A. Piarristeguy, M. Mirandou, M. Fontana, and B. Arcondo, "X-ray analysis of GeSeAg glasses," *Journal of non-crystalline solids*, vol. 273, no. 1-3, pp. 30–35, 2000.

[114] A. Fischer-Colbrie, A. Bienenstock, P. Fuoss, and M. A. Marcus, "Structure and bonding in photodiffused amorphous Ag-GeSe2 thin films," *Physical Review B*, vol. 38, no. 17, p. 12388, 1988.

[115] P. S. Salmon and I. Petri, "Structure of glassy and liquid gese2," *Journal of Physics: Condensed Matter*, vol. 15, no. 16, p. S1509, 2003.

[116] J. Phillips, "Topology of covalent non-crystalline solids I: Short-range order in chalcogenide alloys," *J. Non-Cryst. Solids*, vol. 34, p. 153, 1979.

[117] J. Phillips, "Topology of covalent non-crystalline solids II: Medium-range order in chalcogenide alloys and A- Si (Ge)," *Journal of Non-Crystalline Solids*, vol. 43, no. 1, pp. 37–77, 1981.

[118] M. F. Thorpe, "Continuous deformations in random networks," *Journal of Non-Crystalline Solids*, vol. 57, no. 3, pp. 355–370, 1983.

[119] S. Sugai, "Stochastic random network model in ge and si chalcogenide glasses," *Physical Review B*, vol. 35, no. 3, p. 1345, 1987.

[120] R. Cappelletti, M. Cobb, D. Drabold, and W. Kamitakahara, "Neutron-scattering and ab initio molecular-dynamics study of vibrations in glassy gese 2," *Physical Review B*, vol. 52, no. 13, p. 9133, 1995.

[121] J. Phillips, "Structural Principles of α-AgI and Related Double Salts," *Journal of The Electrochemical Society*, vol. 123, no. 6, pp. 934–940, 1976.

[122] R. Kubo, "The fluctuation-dissipation theorem," *Reports on progress in physics*, vol. 29, no. 1, p. 255, 1966.

[123] A. Piarristeguy, J. C. Garrido, M. Ureña, M. Fontana, and B. Arcondo, "Conductivity percolation transition of Agx (Ge0. 25Se0. 75) 100- x glasses," *Journal of Non-Crystalline Solids*, vol. 353, no. 32-40, pp. 3314–3317, 2007.

[124] T. Abtew, F. Inam, and D. Drabold, "Thermally stimulated h emission and diffusion in hydrogenated amorphous silicon," *EPL (Europhysics Letters)*, vol. 79, no. 3, p. 36001, 2007.

Thesis and Dissertation Services